REPORT DOCUMENTATION PAGE		READ INSTRUCTIONS BEFORE COMPLETING FORM
1. REPORT NUMBER AFIT/CI/NR 88-85	2. GOVT ACCESSION NO.	3. RECIPIENT'S CATALOG NUMBER
4. TITLE (and Subtitle) METHOD FOR OBTAINING EMPIRICAL CORRELATIONS FOR PREDICTING CRACK PROPAGATION IN A BURNING SOLID PROPELLANT GRAIN		5. TYPE OF REPORT & PERIOD COVERED MS THESIS
		6. PERFORMING ORG. REPORT NUMBER
7. AUTHOR(s) JEFFREY A. NIMIS		8. CONTRACT OR GRANT NUMBER(s)
9. PERFORMING ORGANIZATION NAME AND ADDRESS AFIT STUDENT AT: PENNSYLVANIA STATE UNIVERSITY		10. PROGRAM ELEMENT, PROJECT, TASK AREA & WORK UNIT NUMBERS
11. CONTROLLING OFFICE NAME AND ADDRESS		12. REPORT DATE 1988
		13. NUMBER OF PAGES 58
14. MONITORING AGENCY NAME & ADDRESS(if different from Controlling Office) AFIT/NR Wright-Patterson AFB OH 45433-6583		15. SECURITY CLASS. (of this report) UNCLASSIFIED
		15a. DECLASSIFICATION/DOWNGRADING SCHEDULE

16. DISTRIBUTION STATEMENT (of this Report)

DISTRIBUTED UNLIMITED: APPROVED FOR PUBLIC RELEASE

DTIC
ELECTE
AUG 0 4 1988
H

17. DISTRIBUTION STATEMENT (of the abstract entered in Block 20, if different from Report)

SAME AS REPORT

18. SUPPLEMENTARY NOTES

19. KEY WORDS (Continue on reverse side if necessary and identify by block number)

20. ABSTRACT (Continue on reverse side if necessary and identify by block number)

ATTACHED

DD 1 JAN 73 FORM 1473   EDITION OF 1 NOV 65 IS OBSOLETE

ABSTRACT

The importance of crack propagation in solid rocket motors is widely recognized. However, the processes of crack propagation and branching in burning solid propellants are not as yet well understood. These processes could be instrumental in creating large specific surface areas for burning causing rocket motor failure. Numerous samples have been recovered from interrupted-burning experiments. Depending on the pressurization rate and sample geometry, different modes of crack propagation and/or branching were observed. This problem was analyzed through the use of basic physical principles, current theories on crack propagation in viscoelatic media, and experimental results. A set of governing dimensionless parameters which control and characterize the degree of damage was obtained. Key factors influencing the crack combustion, propagation and branching process considered in the dimensional analysis include chamber pressurization rate, initial crack length, initial temperature, sample geometry, and mechanical and thermal properties of the solid propellant. Based on experimental results, a multiple regression analysis was performed to obtain a set of correlations between the dimensionless parameters. The procedures developed in this work demonstrate a methodology for obtaining similar correlations which could be used as guidelines for safe operating conditions of rocket motors.

The Pennsylvania State University

The Graduate School

Department of Mechanical Engineering

A Method for Obtaining Empirical Correlations for Predicting
Crack Propagation in a Burning Solid Propellant Grain

A Thesis in

Mechanical Engineering

by

Jeffrey A. Nimis

Submitted in Partial Fulfillment
of the Requirements
for the Degree of

Master of Science

December 1987

We approve the thesis of Jeffrey A. Nimis.

Date of Signature:

Oct 12, 1987

Kenneth K. Kuo

Kenneth K. Kuo, Distinguished Alumni
Professor of Mechanical Engineering,
Thesis Advisor

Oct 12, 1987

Vigor Yang

Vigor Yang, Assistant Professor of
Mechanical Engineering

Oct 14, 1987

Harold R. Jacobs

Harold R. Jacobs, Professor of Mechanical
Engineering, Head of the Mechanical
Engineering Department

ABSTRACT

The importance of crack propagation in solid rocket motors is widely recognized. However, the processes of crack propagation and branching in burning solid propellants are not as yet well understood. These processes could be instrumental in creating large specific surface areas for burning causing rocket motor failure. Numerous samples have been recovered from interrupted-burning experiments. Depending on the pressurization rate and sample geometry, different modes of crack propagation and/or branching were observed. This problem was analyzed through the use of basic physical principles, current theories on crack propagation in viscoelatic media, and experimental results. A set of governing dimensionless parameters which control and characterize the degree of damage was obtained. Key factors influencing the crack combustion, propagation and branching process considered in the dimensional analysis include chamber pressurization rate, initial crack length, initial temperature, sample geometry, and mechanical and thermal properties of the solid propellant. Based on experimental results, a multiple regression analysis was performed to obtain a set of correlations between the dimensionless parameters. The procedures developed in this work demonstrate a methodology for obtaining similar correlations which could be used as guidelines for safe operating conditions of rocket motors.

TABLE OF CONTENTS

LIST OF TABLES

LIST OF FIGURES

NOMENCLATURE

Symbol	Description
A_b	Burning surface area in the affected region (m^2)
A_{bt}	Total burning surface area (m^2)
A_s	Specific burning surface area (m^2)
a	Total crack length (m)
a_o	Initial crack length (m)
a_T	Time shift factor
b	Propellant Sample thickness (m)
c_p	Constant pressure specific heat
E	Relaxation Modulus, total energy (MPa/J)
$e(x)$	Error interval for the variable x (+/- units of x)
h_p	Enthalpy of the propellant (J/Kg)
h_t	Stagnation enthalpy of product gases (J/Kg)
K_I	Stress intensity factor (MPa$\sqrt{m}$)
K_{I_C}	Critical stress intensity factor (MPa$\sqrt{m}$)
L_D	Length of extended macrocrack (m)
$\dot{m}$	Mass flow rate (Kg/s)
n	Number of macrocracks
P	Pressure (MPa)
$\dot{Q}$	Heat loss (J/s)
R^2	Sample multiple coefficient of determination
r_b	Propellant burning rate (m/s)
r_x	Relative error in the dimensionless parameter x
t	Time (s)
T	Temperature (K)

V	Voltage (Volts)
V_a	Affected volume (m^3)
V_c	Chamber free volume (m^3)
V_p	Crack propagation velocity (m/s)
α_p	Thermal diffusivity of propellant (m^2/s)
γ	Ratio of specific heats
Γ	Fracture energy (J/m^2)
ε	Strain
ξ	Shifted time (s)
ν	Poisson's ratio
ρ_p	Density of propellant (Kg/m^3)
$\pi_{()}$	Dimensionless parameter
σ	Stress (MPa)
σ_{fm}	Maximum stress in the failure zone (MPa)
ψ_i	Crack cavity angle (degrees)
ψ_o	Outside taper angle (degrees)

ACKNOWLEDGEMENTS

Chapter 1

INTRODUCTION

1.1 Motivation and Objectives

Solid propellant rocket safety is a key factor in several of today's most important civilian and military propulsion systems. With both civilian and military agencies presently pursuing solid rocket booster safety and ballistic risk assessment programs, near-term advances in this area are foreseeable. Of particular concern is overpressurization and subsequent catastrophic failure of a rocket motor due to anomalous burning, which may be caused by the presence of voids, cracks, or debonded regions in the propellant grain. Such regions are susceptible to further damage under transient loading conditions. A theoretical model has been developed to predict the flame spreading and combustion processes inside a propellant cavity[1] and various models have also been developed for crack initiation and growth in viscoelastic, inert material.[2-5] However, the coupling effects of these two processes are complicated and not totally understood. Based on previous work by Kuo and co-workers[6-8] on crack growth in burning propellant grains, a set of governing dimensionless parameters have been identified to obtain empirical correlations.

The primary objectives of this research are:

a) to define a group of meaningful dimensionless parameters for characterizing the operating conditions and resulting damage of a solid propellant sample;

b) to obtain test data necessary for developing correlations between the dimensionless parameters; and,

c) to establish correlations, demonstrating a methodology for generating useful safety criteria.

1.2 Brief Survey of Related Work

Early studies of the crack propagation phenomena under burning conditions by Siefert and Kuo[6] provided good insight into the basic mechanisms involved. They studied the crack propagation process of a burning propellant sample of constant geometry under varying pressurization rates. Experimental evidence supported the assumption that the crack propagation velocity was limited by the rate of deformation of the crack cavity walls. In this case, a critical stress state was maintained in the failure zone at the crack tip. A nearly linear relationship between the crack velocity and pressurization rate was observed,

$$V_p(m/s) = 0.086[dp/dt(MPa/s)]^{0.637} \tag{1}$$

For low pressurization rates, the crack tip maintained its original contour. However, at pressurization rates on the order of 20 GPa/s, the crack tip appeared to square off and a fan structure developed suggesting the occurrence of crack branching and microstructure damage. It is interesting to note that the maximum crack velocities measured correspond to terminal velocities of inert propellants and rubber reported by Gent and Marteny.[9]

Further studies by Kuo, Moreci and Mantzaras[7,8] have identified four different modes of damage which were related to the pressurization rate of the crack cavity. Figure 1 shows the measured crack propagation velocity as a function of pressurization rate and where each of these
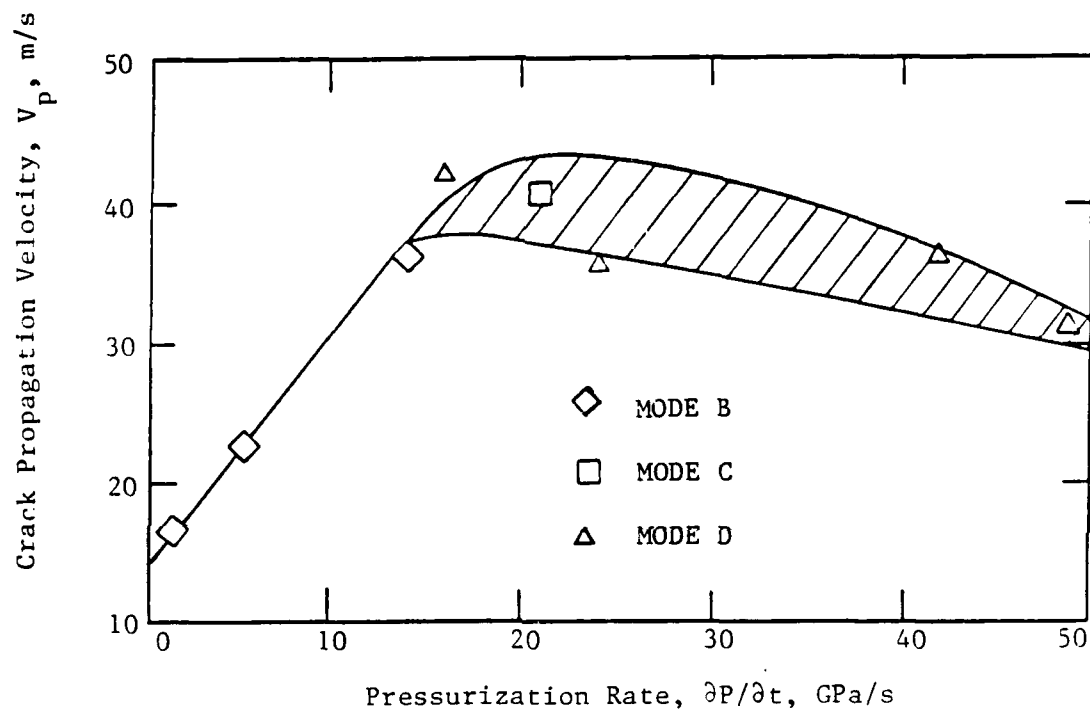
Fig. 1 Crack Propagation Velocity versus Pressurization Rate

modes was observed. Mode A represents little or no increase in crack length and corresponds to very low pressurization rates. No departure from normal burning is expected for this case. Mode B represents the propagation of a single crack. The rate of crack growth increases almost linearly with pressurization rate in the range of 1.4 to 15.0 GPa/s. Although burning is enhanced at the crack tip, the overall increase in burning due to the damage is not significant. Mode C represents an initial single crack propagation with local branching at various locations. This was observed for intermediate pressurization rates and has the potential of significantly increasing the burning surface area. Mode D represents crack branching from the initial crack tip location in either discrete macrocracks or a fan of numerous smaller cracks. This type of damage was characteristic of higher pressurization rates and also can significantly increase the burning surface area. Some of the data from these experiments, as well as newly acquired data, were used in the current analysis.

Chapter 2

EXPERIMENTAL SETUP

2.1 Selection of Sample Propellant Type

In selecting a propellant sample for this research, the following
criteria were considered:

a) the propellant must be available for a basic study in a
university environment;

b) its combustion behavior must be well characterized;

c) its mechanical properties and failure criterion under non-buring
conditions must be known.; and,

d) propellants of the same family must be available so that similar
tests can be conducted to determine the effect of burning rate and
oxidizer size.

Two composite propellants (ARC 5051 and ARC 4525) were selected.
Each of these contain 27% HTPB and 73% AP with average oxidizer particle
sizes of 200μm (ARC 5051) and 20μm (ARC 4525). Due to the similarities
in composition thermodynamic properties such as enthalpy, density,
burning rate, etc., are nearly equal. Their combustion behavior and
mechanical properties have been well characterized. In addition,
propellants of similar compostion but with different burning rates are
available for future studies. Although these propellants have a lower
solids loading than the typical high-energy solid propellants used in
most of today's advanced rocket propulsion systems, once the basic
method for determining crack combustion correlations has been
established, similar studies can be made for other propellants.

2.2 Sample Configuration

The two-dimensional sample configuration used in previous studies is adopted for this study (Fig. 2). This general geometry is similar to one point of a star grain or to a segment of a grain containing a void. This configuration provides an initial crack of variable length and propagation along the horizontal axis. The geometric parameters ψ_o and ψ_i can also be varied to represent different local boundary conitions of the damaged zone.

2.3 Test Setup

The test setup was designed to induce combustion and mechanical damage in a localized zone of a pre-cut propellant sample by subjecting it to high-pressure, high-temperature gases and to interupt the buring by rapid depressurization for sample recovery. In these tests variations of several independent parameters were made, including pressurization rate, initial crack length, sample geometry and propellant composition. The damage was then measured in terms of crack propagation velocity, extended crack length and number of cracks.

2.3.1 Test Chamber

The test rig (Fig 3) consisted of a high-pressure, windowed chamber with the following subsystems:

a) a driving motor to pressurize the free volume of the chamber;

b) a rupture disk and venting port to rapidly depressurize the chamber; and,

c) a nitrogen injection system to cool the exposed surfaces and reduce the chance of sample reignition.
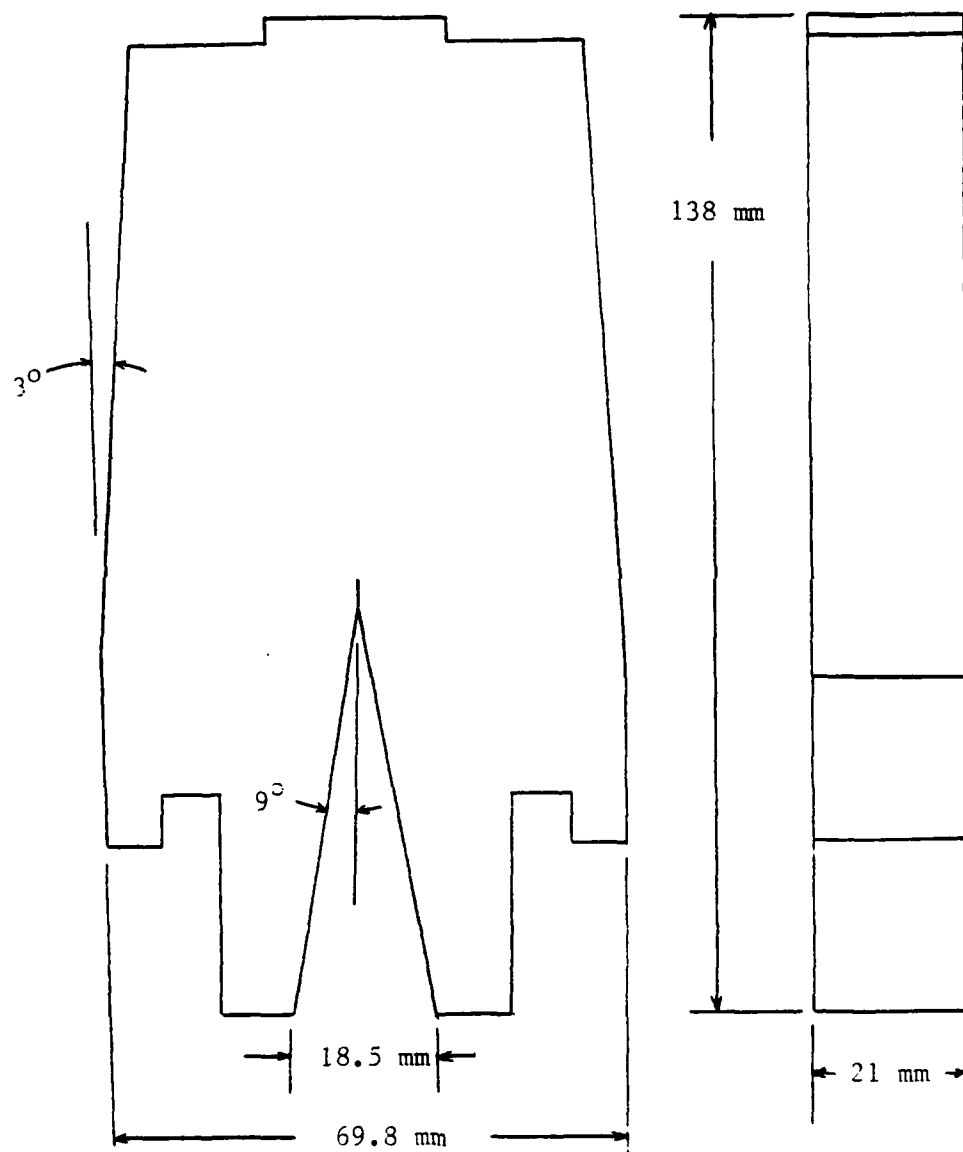
Fig. 2 Propellant Sample Configuration Before Loading

Rupture Disk

Pressure
Transducers

Propellant
Sample

Nitrogen
Injection
System
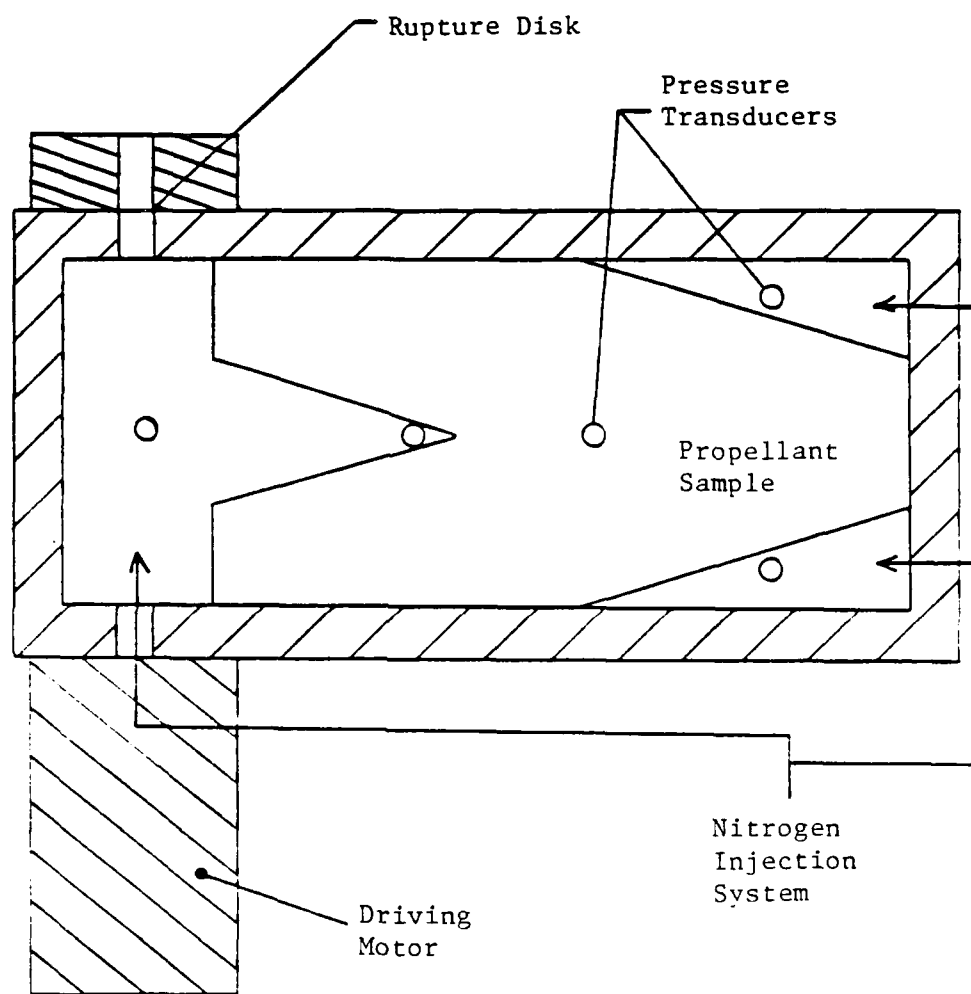
Driving
Motor

Fig. 3   Test Chamber Schematic

2.3.1.1 Driving Motor

The driving motor contained four key components (Fig 4). The ignition primer (type M52A3B1), when supplied with three to four volts DC, would fire and in turn ignite the propellant shavings. The shavings burn extremely fast due to their very high burning surface area. Their purpose was to supply hot gases and boost the pressure in the segment containing the main igniter charge. The igniter charge would then burn, exhausting through the perforated nozzle into the main chamber. By varying the mass of the main igniter charge, pressurization rates ranging from near zero to 50 Gpa/s were achieved.

2.3.1.2 Rupture Disk and Venting Port

When the chamber pressure exceeds a predetermined value the brass rupture disk bursts, allowing the high pressure gases to escape through the venting port. As described by De Luca,[10] dynamic extinction can be achieved by exceeding a critical depressurization rate. This rate increases as chamber pressure increases and is also substantially affected by propellant composition. Due to its complexity, no attempt was made to characterize the extinction properties of the test propellants. Instead, an exit port area of 2.54 cm^2, based on experimental data of Kuo and Moreci,[7] used with rupture pressures between 7.0 and 15.0 MPa proved to be sufficient.

2.3.1.3 Nitrogen Injection System

After the rupture disk bursts and the chamber pressure is reduced, hot spots on the chamber walls could reignite the propellant surfaces and the sample would be completely consumed. In an effort to improve the reliability of interrupting the burning process, nitrogen was
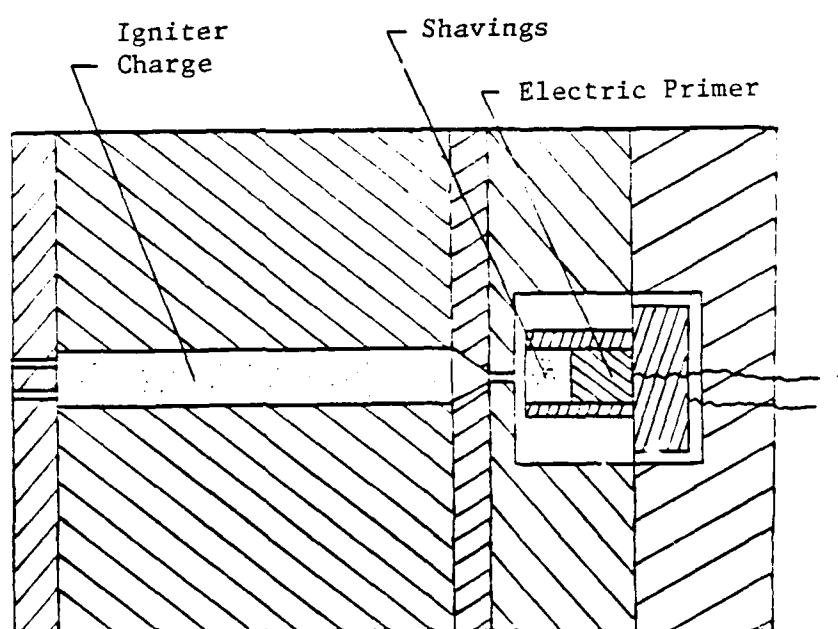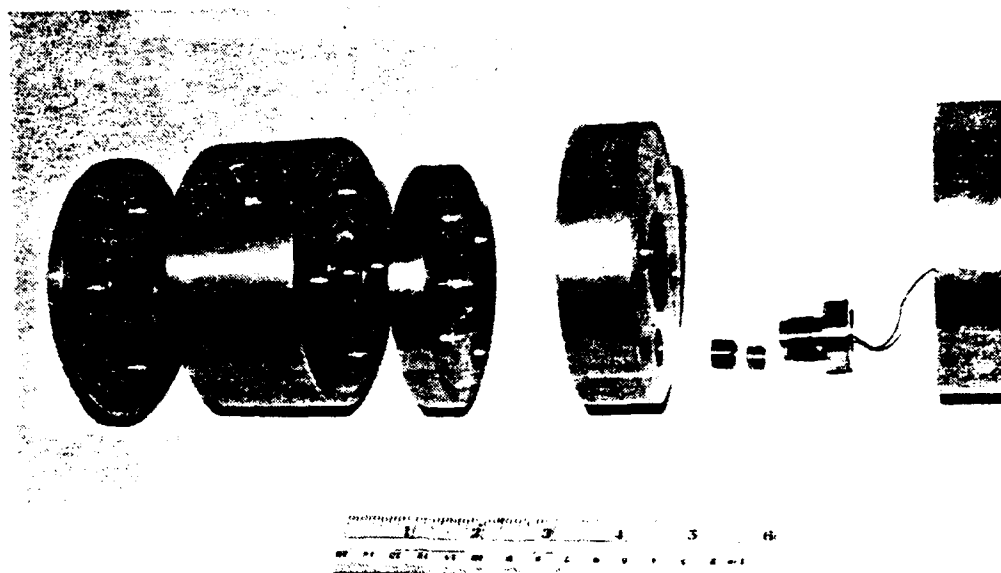
Fig. 4 Driving Motor

injected following depressurization to cool the surfaces of the free volume.

2.3.2 Data Acquisition System

The data needed from these tests to calculate key parameters consisted of a pressure-time trace of the crack cavity as well as a visual record of the crack itself as it propagated. A complete schematic of the data acquisition system is shown in Fig 5.

2.3.2.1 Pressure Measurements

The pressure measuring device selected was a miniature piezoelectric quartz transducer (Kistler Model 601B1). This transducer has a 10% to 90% rise time of 3.0 microseconds over the range of 0 to 15,000 psi. This was more than adequate for measuring pressurization rates of up to 50 GPa/s with rise times on the order of 1 millisecond. To protect the transducers from the high temperature product gases, they were recess-mounted in water-cooled adapters. An insulated high-impedence cable with a nominal capacitance of 30 pF/ft was used to transmit the signal from the transducer to the charge amplifiers. The signal attenuation under the test conditions was less than one percent.

The charge amplifiers (Kistler Model 504E) output the transducer charge signal as an amplified voltage. Calibration is achieved in the charge amplifier by supplying a DC voltage of equal magnitude to that of the pressure transducer sensitivity. The output voltage of the charge amplifier is then adjusted to satisfy the equation

$$V_{out} = \frac{-V_{in} \times 1000pF}{Range \times Sensitivity} \tag{2}$$

A typical range setting of 2000 psi/volt resulted in a calibration
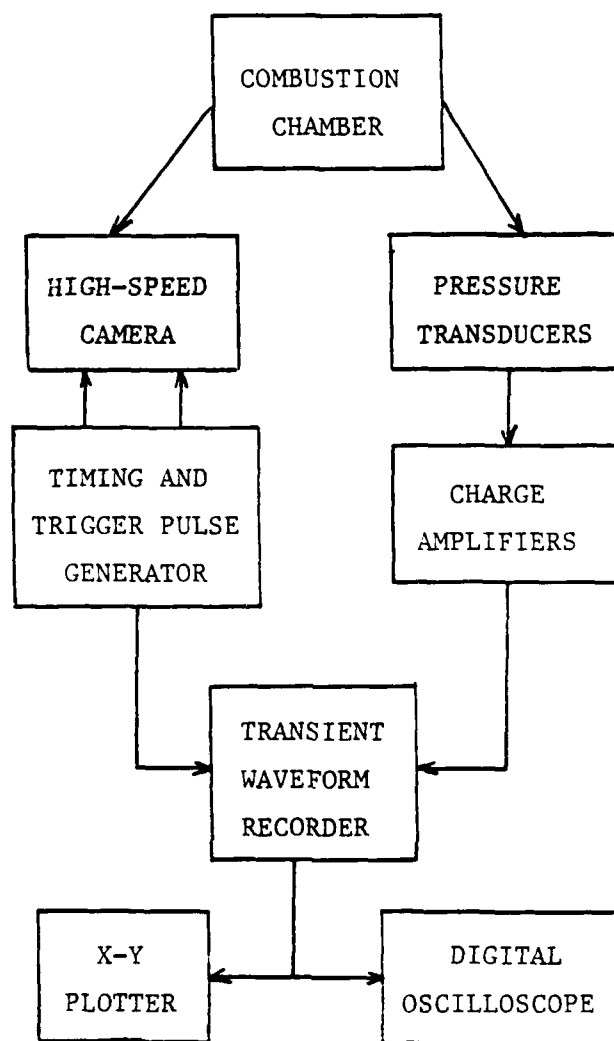
Fig. 5 Data Acquisition System

output of 0.5 volts. A long time constant was used to provide a continuous signal.

The output from the charge amplifiers was recorded on a Physical Data Model 515A Transient Waveform Recorder. It recorded the voltage signals at sampling intervals of 5 to 50 microseconds for the initial pressurization period and then shifted to a sampling rate of 2.5 to 5 milliseconds in order to extend the total time recorded. The limiting factor was its maximum capacity of 4096 data points. The recording mechanism was triggered by a small signal from the transducer in the crack cavity. A negative delay of 512 data points was used to insure the beginning of the event was recorded. The recorded signal could then be played back to a Nicolet Digital Oscilloscope for analysis and recording on floppy disk or to an X-Y plotter for a hardcopy.

2.3.2.2 High Speed Film Recording

A Hycam, 16 mm camera was used to record the ignition, combustion, and crack propagation of the propellant sample through a veiwing port in the chamber. Typical framing rates were 5,000 frames per second in a half frame format resulting in 10,000 pictures per second. In order to insure the event occurred before the roll of film was completely exposed, the camera was used to trigger the ignition of the driving motor. The camera was started and when a prescribed footage of film was exposed, allowing the camera to reach the set film speed, an internal switch would close the igniter circuit. This would also trigger a common time pulse which was recorded both on the film and on the Physical Data Recorder. Another light pulse with a frequency of 1 KHz was also recorded on the film, to one side of the main image, in order

to verify the framing rate.

2.4 Test Procedure

Appendix A contains a complete checklist and sample data sheet used for the interrupted crack propagation tests. The following is a brief description of 'he key steps in a typical test firing:

a) measure the main ignitor charge and shavings and assemble ignitor. Measure the resistance of the primer and short the primer circuit;

b) measure and record the crack geometry of the propellant sample. Cover all surfaces, except crack cavity, with flame retardant grease to prevent flame spreading over those surfaces. Install the sample and bolt on the window and retainer;

c) install pressure transducers and calibrate the charge amplifiers. Connect amplifier outputs to the Physical Data recorder;

d) set up the high-speed camera and test ingition circuit;

e) put charge amplifiers in the OPERATE position, reset the Physical Data recorder and start the camera;

f) when the rupture disk bursts, open the nitrogen line;

g) turn off charge amplifiers, store and plot the pressure traces and disassemble the chamber to examine the recovered sample.

Chapter 3

THEORETICAL ANALYSIS

3.1 Crack Sample Geometry

Figure 6 shows the damaged sample geometry considered in this analysis. From this geometry, some key parameters can be defined. First, $_o$ and $_i$ are direct geometric factors affecting the crack propagation process, and the number of cracks n, is a key factor in defining the degree of damage.[11] The affected volume, or damaged-zone volume is defined as

$$V_a = \pi L_D^2 b \tag{3}$$

The burning surface surface area in the affected region is given by

$$A_b = 2\pi (n+1) L_D b \tag{4}$$

For this analysis, a specific burning surface area is defined as

$$A_s = \frac{A_b}{V_a} = \frac{2(n+1)}{L_D} \tag{5}$$

The functional forms of equations (3) and (5) are

$$V_a = V_a(L_D, b) \tag{6}$$

$$A_s = A_s(L_D, n) \tag{7}$$

3.2 Determination of Mechanical Properties

A series of mechanical tests was conducted by Harbert and Schapery[12] to determine the mechanical properties of the two propellants
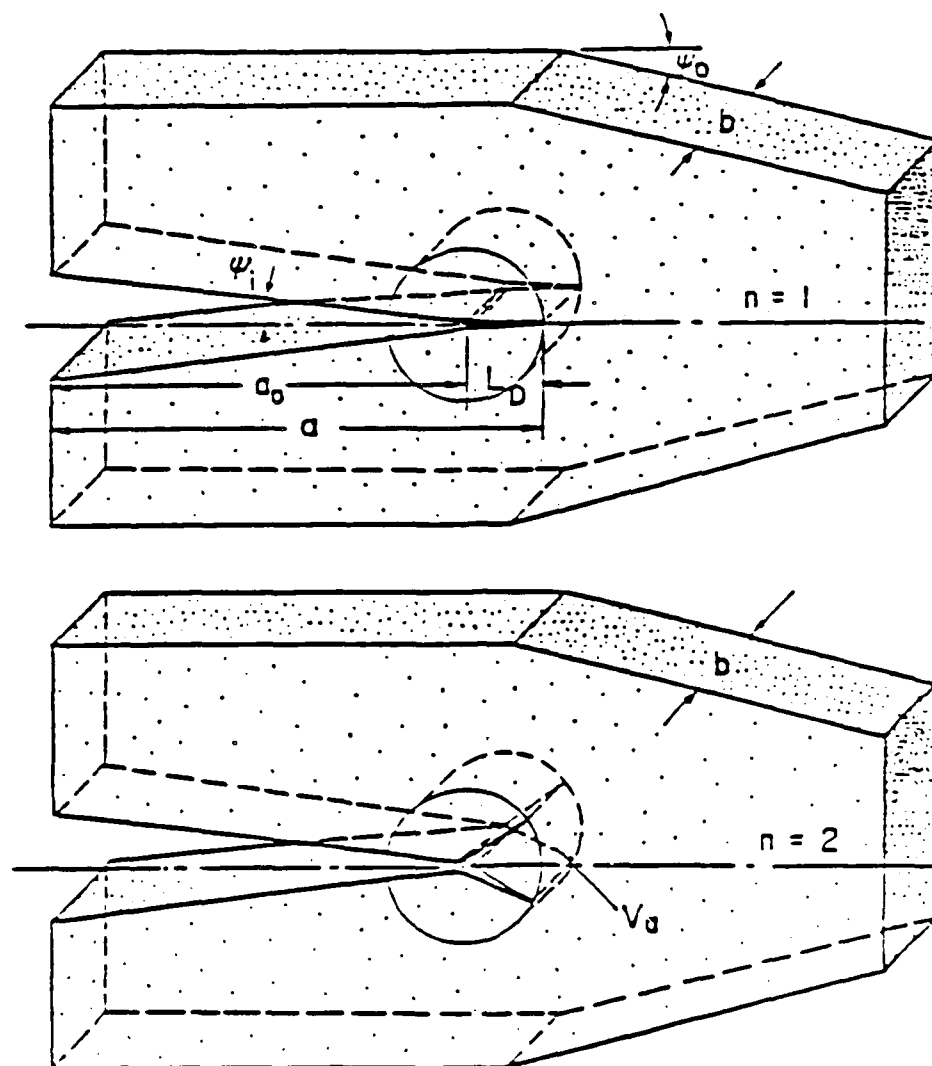
Fig. 6 Geometry of the Damaged Propellant Sample

(ARC 5051 and ARC 4525) under non-burning conditions.

3.2.1 Relaxation Modulus

Uniaxial constant strain tests on propellant bar specimens were performed at various temperatures. Relaxation moduli versus time data are plotted for each temperature. In order to obtain a continuous curve for all temperatures, the relaxation moduli are plotted versus a shifted time ξ, where

$$\xi = t/a_T \qquad (8)$$

The time shift factor a_T was determined based on a reference temperature of 297 K (i.e., $a_T = 1.0$ at 297 K). Figure 7 shows the functional relationship between temperature and time shift factor. The resulting master relaxation curve for each propellant is shown in Figure 8.

3.2.2 Crack Propagation Velocity

Crack growth tests were conducted on strip specimens with a precut crack (Fig. 9) at different crosshead rates. The crack velocity and strain were measured directly and the stress intensity was calculated using

$$K_I = \sigma\sqrt{h/2(1-\nu^2)} \qquad (9)$$

where Poisson's ratio $\nu = 0.5$ and σ is the stress far from the crack tip exerted by the crosshead.[13] Figure 10 shows the relationship between crack propagation velocity and stress intensity factor for ARC 4525 propellant. It can be seen that the lines of constant strain are parallel (i.e., independent of strain). This fact suggests the applicability of linear viscoelastic theory to characterize the crack propagation velocity.[14] The results of this theory can be expressed by
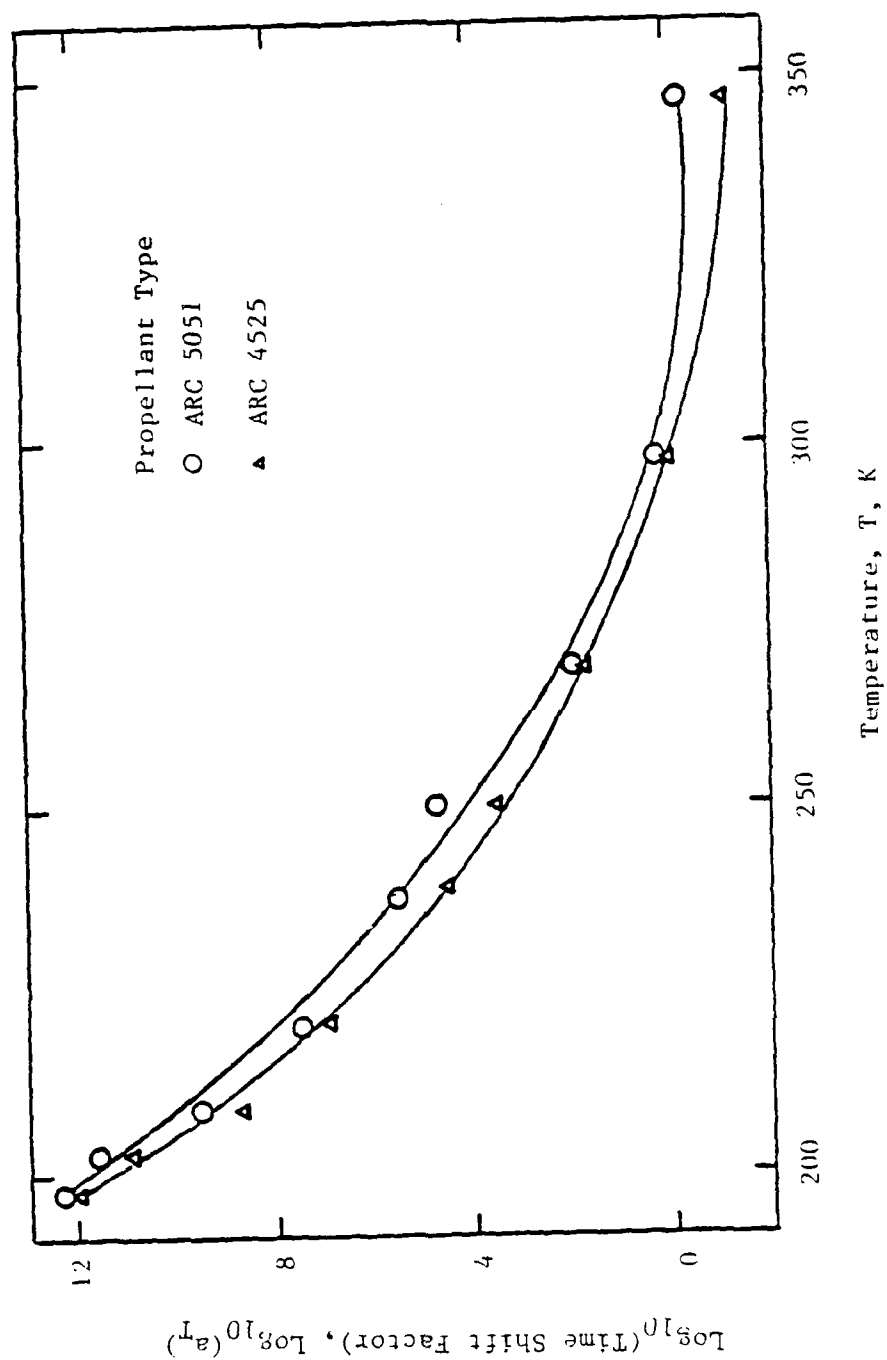
Fig. 7 Time Shift Factor versus Temperature
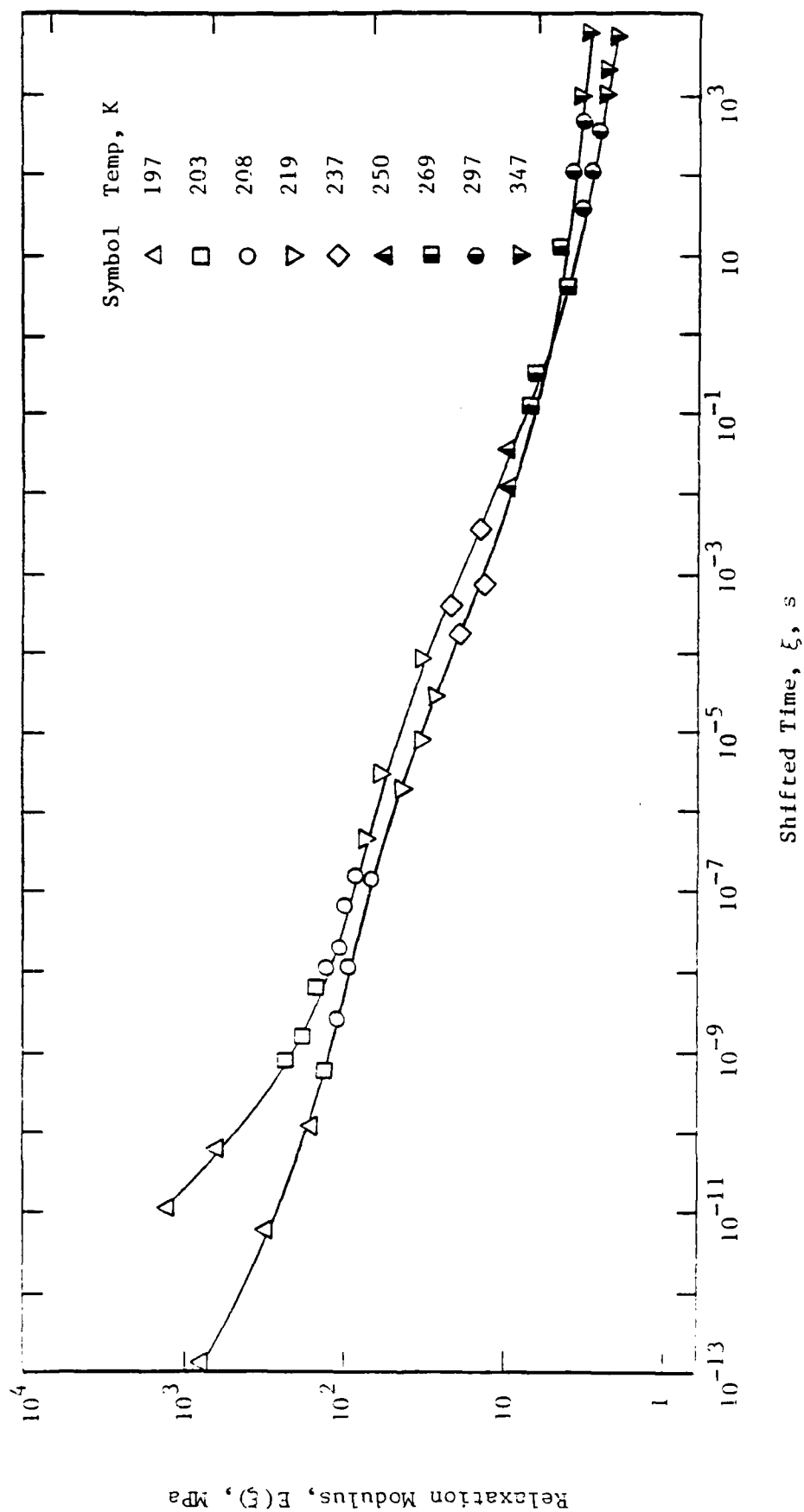
Fig. 8 Master Relaxation Curve
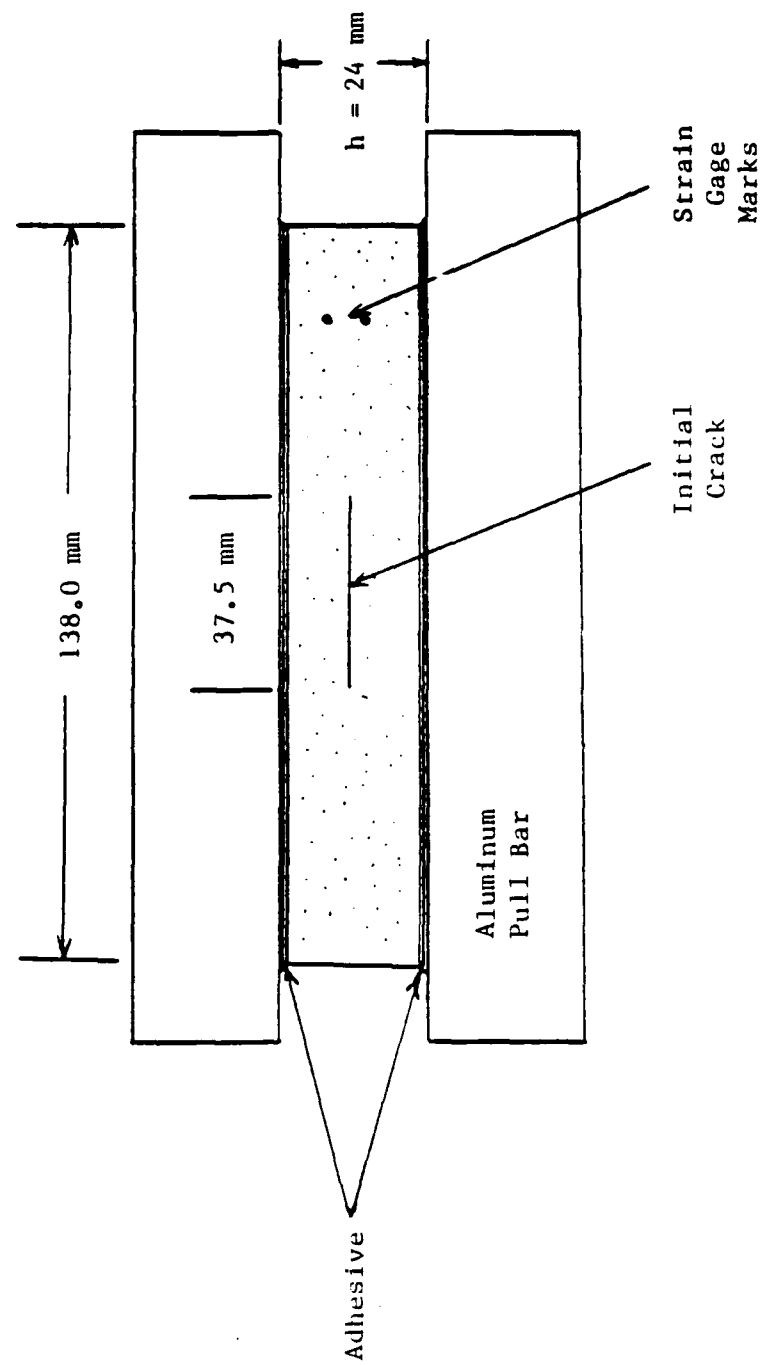
Fig. 9 Strip Test Specimen for Crack Propagation Velocity Characterization
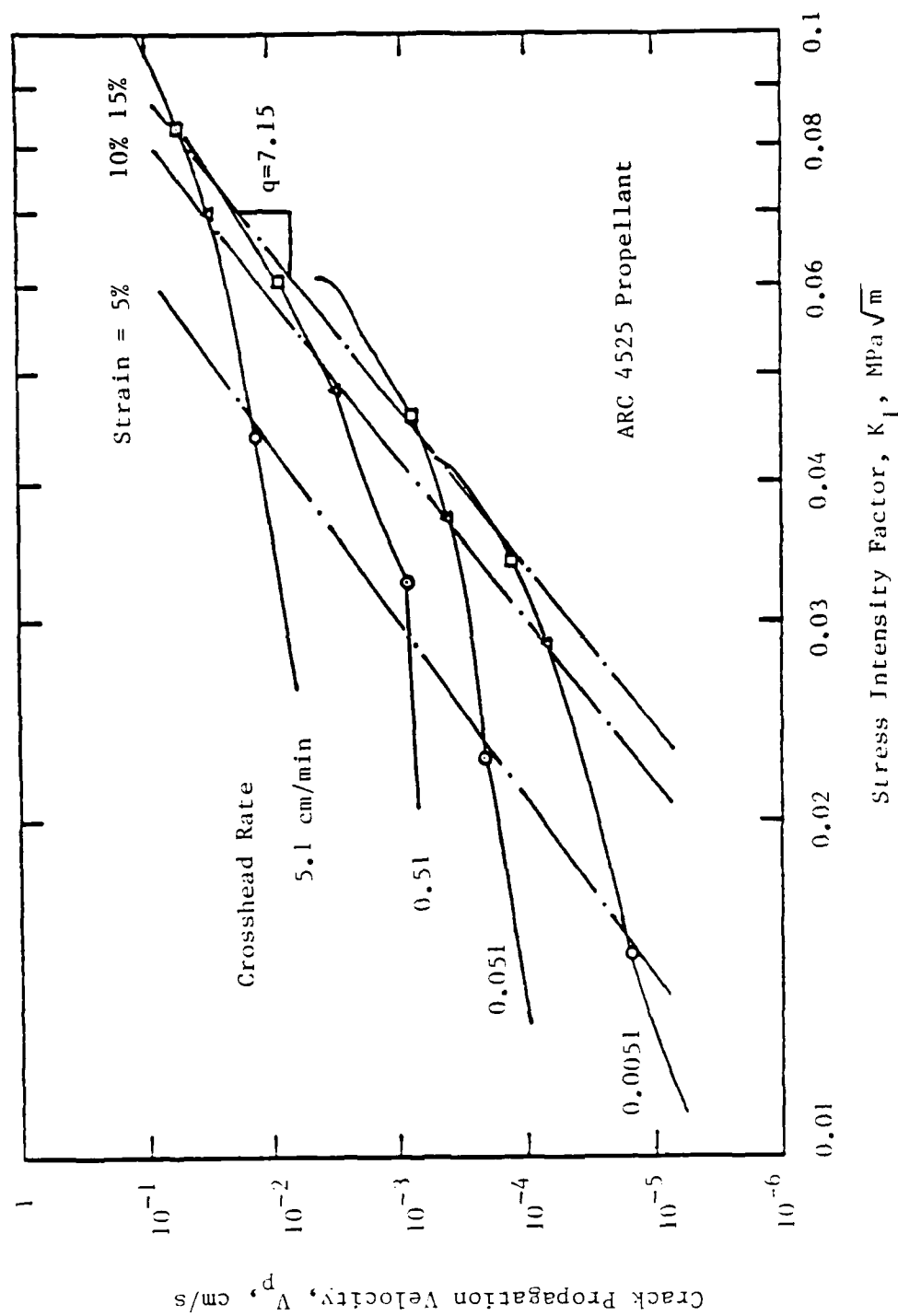
Fig. 10 Crack Propagation Velocity versus Stress Intensity Factor for ARC 4525

the following power law

$$V_p = \frac{C}{a_T}(K_I)^q \qquad (10)$$

In this equation q is the strain-independent slope obtained from Figure 10, and C is a material parameter which varies with strain. The functional representation of equation (10) is then

$$V_p = V_p(K_I, \epsilon, a_T) \qquad (11)$$

3.2.3 Fracture Energy and Related Parameters

From an idealized crack propagation model for viscoelastic media as used by Knauss[2] and Schapery[3-5], the fracture energy (Γ) can be defined as the energy required to elongate a segment of area dA to the point of failure. This quantity has the functional relationship

$$\Gamma = \Gamma(K_I, V_p, \sigma_{fm}) \qquad (12)$$

where σ_{fm} is the maximum stress in the failure zone. The stress intensity factor is generally a function of the geometry of the continuum in which the failure zone is embedded and the stress in that zone, represented by chamber pressure in this application. Thus

$$K_I = K_I(a_o, \psi_o, \psi_i, P) \qquad (13)$$

and

$$K_{I_C} = K_I \qquad (14)$$

for crack initiation. From Langlois and Gonard,[15] the extended crack length can be related to stress intensity factor and the maximum stress in the failure zone

$$L_D = L_D(K_I, \sigma_{fm}) \qquad (15)$$

3.3 Energy Balance on the Control Volume

An energy balance is applied to the control volume (Figure 11) in order to relate key parameters in the combustion process. The basic assumptions are:

a) The heat loss from the control volume to the surroundings is negligible since the damage occurs in an extremely short time interval (of the order of 10 ms).

b) The combustion gases of the driving motor are considered to follow the perfect gas law. This assumption is valid since the gas temperature is high (2000 K) and the maximum chamber pressure is less than 35 MPa.

c) $\dot{m}_{out} = 0$ for the time of interest since the initial damage occurs before the rupture disk bursts.

d) The gas phase control volume can be treated as a constant since the volume increase due to flow work and surface burning is extremely small compared to the total control volume during the time of interest. The conservation of energy for the gas phase can be written as

$$\frac{\partial E}{\partial t} = \dot{m}_{ign} h_{t,ign} + \dot{m}_p h_p - \dot{m}_{out} c_p T - \dot{Q} - P \frac{\partial V_c}{\partial t} \tag{16}$$

Using the basic assumptions, equation (16) reduces to

$$\frac{V_c}{\gamma - 1} \frac{\partial P}{\partial t} = \dot{m}_{ign} h_{t,ign} + \dot{m}_p h_p \tag{17}$$

After replacing $\dot{m}_p$ according to

$$\dot{m}_p = \rho_p r_b A_{bt} \tag{18}$$

24
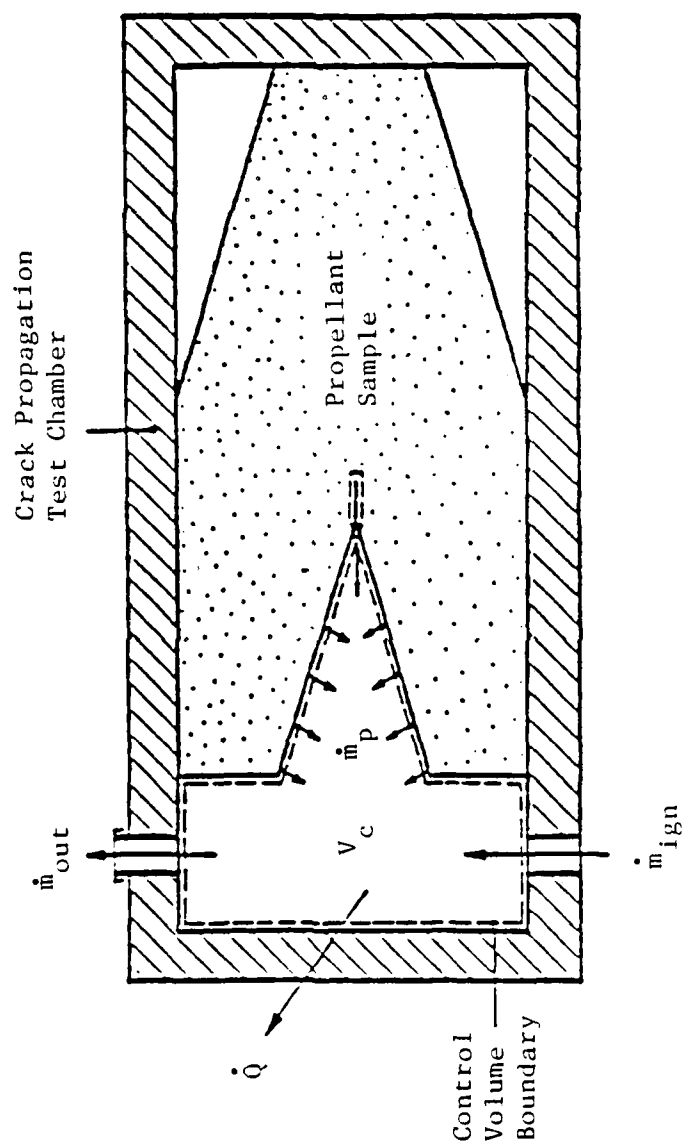
Fig. 11 Control Volume Used in Energy Analysis

where the total burning surface area A_{bt} can further be related to the crack geometry

$$A_{bt} = A_{bt}(V_a, A_s, L_D, a_o, \psi_i) \tag{19}$$

Equation (17) then takes on the functional form

$$\frac{\partial P}{\partial t} = \frac{\partial P}{\partial t}(V_c, \dot{m}_{ign}, h_{t,ign}, r_b, V_a, a_o, L_D, \rho_p, \psi_i, A_s, h_p) \tag{20}$$

The burning rate under a pressure transient has been characterized by Krier[16] as

$$r_b(t) = r_o[1 + \frac{\phi n \alpha_p}{P(t)r_o^2} \frac{dp}{dt}] \tag{21}$$

where r_o is the steady state burning rate according to the Saint-Robert law,[17] α_p is the solid phase thermal diffusivity, and n and ϕ are numerical constants. Since the thermal diffusivities were the same for both propellants[12] it also was treated as a numerical constant. The instantaneous burning rate can therefore be related as

$$r_b = r_b(P, \partial P/\partial t) \tag{22}$$

Since the flow from the driving motor is choked and the ignitor charge is made of the same propellant as the sample, the propellant enthalpy can be related to the stagnation enthalpy of the igniter gases as

$$h_p - \frac{2}{\gamma-1} h_{t,ign} \tag{23}$$

The propellants are essentially incompressible and of equal density, therefore

$$\rho_p = \text{constant} \tag{24}$$

From evidence obtained in crack propagation experiments,[11] crack propagation velocity in the burning solid propellants is related to the following parameters:

$$V_p = V_p(\partial p/\partial t, P, \dot{m}_{ign}, \Gamma, \psi_o, \psi_i, V_c, A_s, a_o, a_T) \tag{25}$$

3.4 Dimensional Analysis

Equations (6), (7), (11)-(15), (20) and (22)-(25) relate the twenty-three parameters (γ was assumed to be a numerical constant for the combustion product gases) affecting the crack propagation process. These twelve equations may be reduced to one equation involving twelve of the more significant parameters, namely

$$V_p = V_p(\partial P/\partial t, r_b, a_o, h_p, K_{I_C}, V_a, A_s, L_D, \psi_o, \psi_i, a_T) \tag{26}$$

3.4.1 Arrangement into Meaningful Dimensionless Groups

The Buckingham Pi Theorem[18] indicates that there exist nine independent dimensionless parameters involved in the crack propagation process. Three of the key parameters are already dimensionless, thus ψ_o, ψ_i and a_T were chosen as dimensionless parameters describing the geometry of the continuum around the damaged zone and the effect of initial propellant temperature on mechanical properties. In order to develop additional meaningful groups, the parameters which describe the degree of damage (i.e., L_D, V_a, A_s and V_p) were examined individually.

A desireable dimensionless parameter defining the extended crack length was the percentage increase in overall crack length. This dimensionless parameter was defined as

$$\pi_A = \frac{L_D}{a_o} = \frac{\text{Length of extended macrocrack}}{\text{Length of the initial crack}} \qquad (27)$$

From the parameters V_a and A_s, two meaningful dimensionless groups could be formed,

$$\pi_B = \frac{V_a A_s^2}{2L_D} = \frac{\text{Rate of increase of crack surface area}}{\text{Rate of increases of cross-sectional area of the affected region}} \qquad (28)$$

$$\pi_C = \pi A_s L_D - 1 = n, \text{ number of macrocracks of length } L_D \qquad (29)$$

The crack propagation velocity was normalized to the normal regression rate of the surface due to burning,

$$\pi_D = \frac{V_p}{r_b} = \frac{\text{Crack propagation Velocity}}{\text{Burning rate of the main propellant}} \qquad (31)$$

The remaining dimensionless parameters relate the input energy from the propellant and the presurization rate to the critical values for crack propagation and were grouped as follows:

$$\pi_E = \frac{h_p \rho_p r_b A_s \pi L_d^2}{V_p [K_{I_C}^2 (1-\nu^2)/E_{ref}]} = \frac{\text{Rate of thermal energy input from propellant product gases}}{\text{Strain energy release rate required for crack propagation}} \qquad (32)$$

$$\pi_F = \frac{\frac{\partial P}{\partial t} L_d^{3/2}}{K_{I_C} r_b} = \frac{\text{Rate of change of pressure force exerted on the crack surface}}{\text{(critical stress for fracture)}\times\text{(rate of increase of flow area in the damaged zone)}} \qquad (33)$$

The additional constants such as density, sample thickness and Poisson's ratio were added to give the groups their respective physical meaning.

3.4.2 Functional Relationships Between Dimensionless Parameters

The dimensionless parameters π_A, π_B, π_C, π_D characterize the degree of damage in the propellant sample. The driving force causing this damage (i.e., the initial pressurization rate and thermal energy input from the propellant gases) are characterized by the dimensionless parameters π_E and π_F. These parameters were used together with ψ_o, ψ_i and a_T for constructing the following emperical correlations to predict the crack propagation and branching processes:

$$\pi_A = \pi_A(\pi_E, \ \pi_F, \ \psi_o, \ \psi_i, \ a_T)$$
$$\pi_B = \pi_B(\pi_E, \ \pi_F, \ \psi_o, \ \psi_i, \ a_T)$$
$$\pi_C = \pi_C(\pi_E, \ \pi_F, \ \psi_o, \ \psi_i, \ a_T)$$
$$\pi_D = \pi_D(\pi_E, \ \pi_F, \ \psi_o, \ \psi_i, \ a_T)$$

$$(33)$$

Chapter 4

RESULTS

4.1 Determination of Dimensionless Parameters

Several tests were conducted using the aparatus previously

described. From the pressure data, film data and known mechanical and

thermodynamic properties, values for each of the parameters could be

deduced.

4.1.1 Pressure Loading in the Damaged Zone

Figure 12 shows the pressure-time trace at three key locations in

a typical test. Location 1 corresponds to the chamber free-volume and

location 2 corresponds to the initial crack tip location and the 3rd is

further along the crack propagation direction. The first curve is the

driving pressurization rate used in calculating the dimensionless

parameters since it is generally independent of the initial crack

configuration. The pressure trace for the second location illustrates

the increased pressurization rate and peak pressure experienced at the

tip of an opening crack. This may be caused by the delayed opening of

the crack and/or the increased burning rate in the failure zone. As

seen, the peak pressure in this case was 13.8 MPa (2000 psi) when the

rupture disk burst. The chamber pressure then dropped rapidly, and the

sample was recovered. Figure 13 is a close-up photograph of the

damaged zone showing the bracnching which occurred.

Figure 14 is a similar pressure trace for another test. The

rupture disk burst earlier in this case (7.0 MPa), which may have

contributed to the reignition and burn-out of the sample. The early
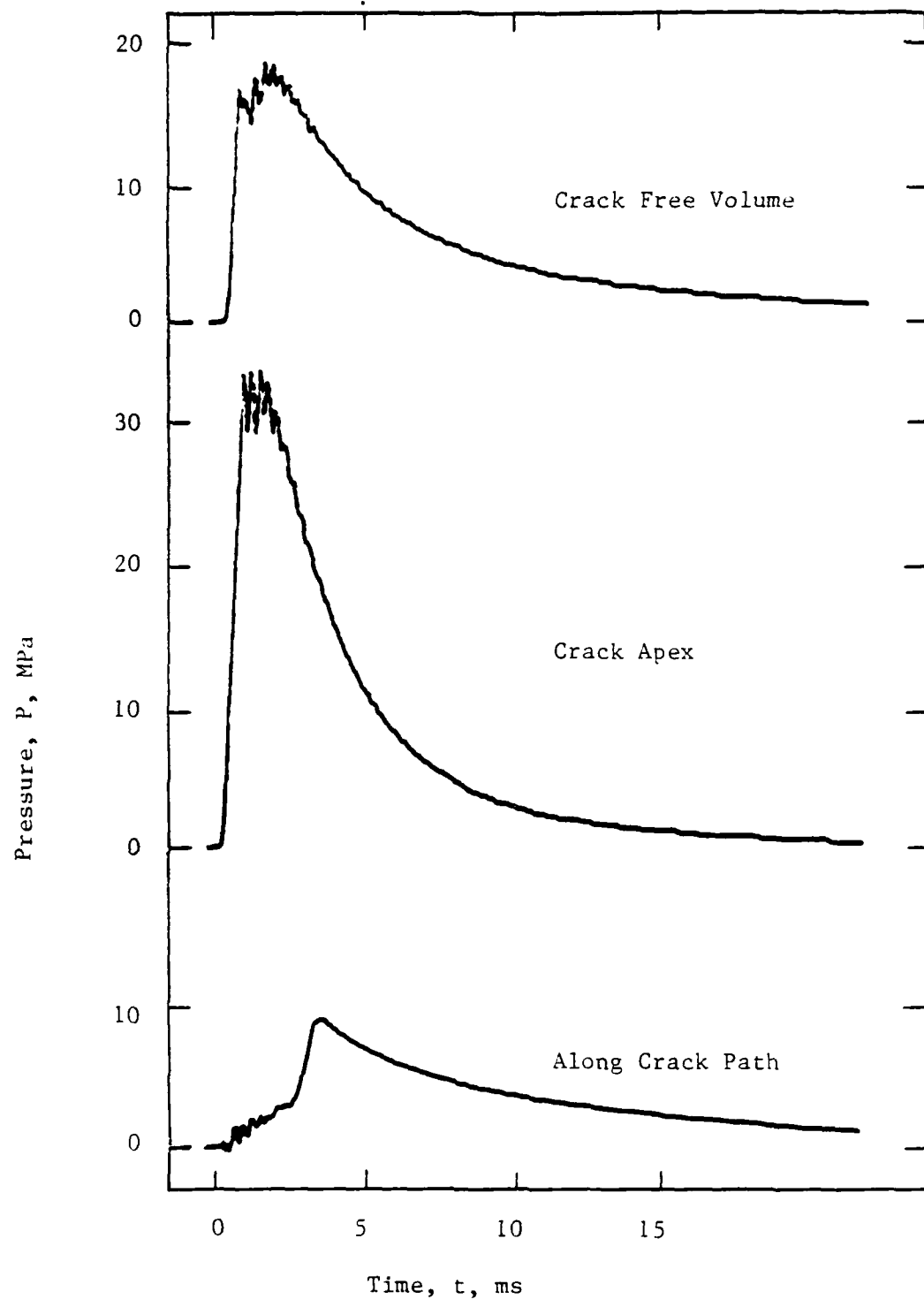
Fig. 12   Pressure–Time Trace for DNICP 27
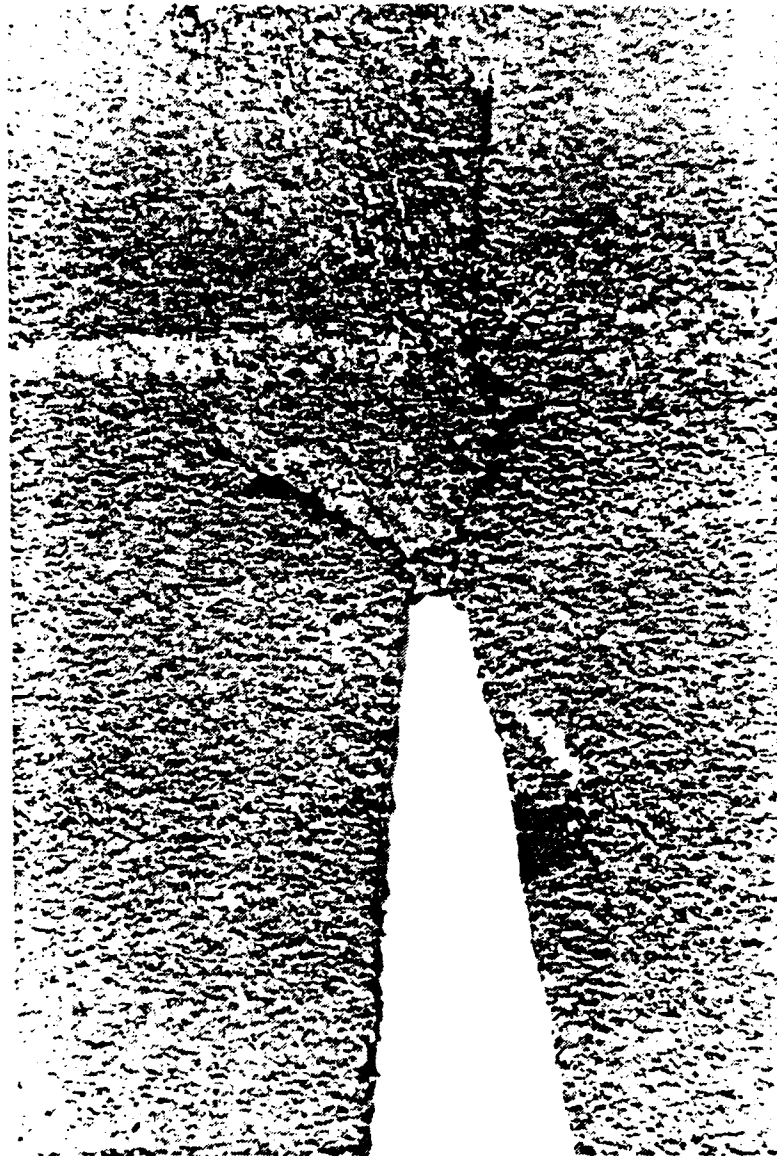
Fig. 13 Recovered Sample from DNICP 27
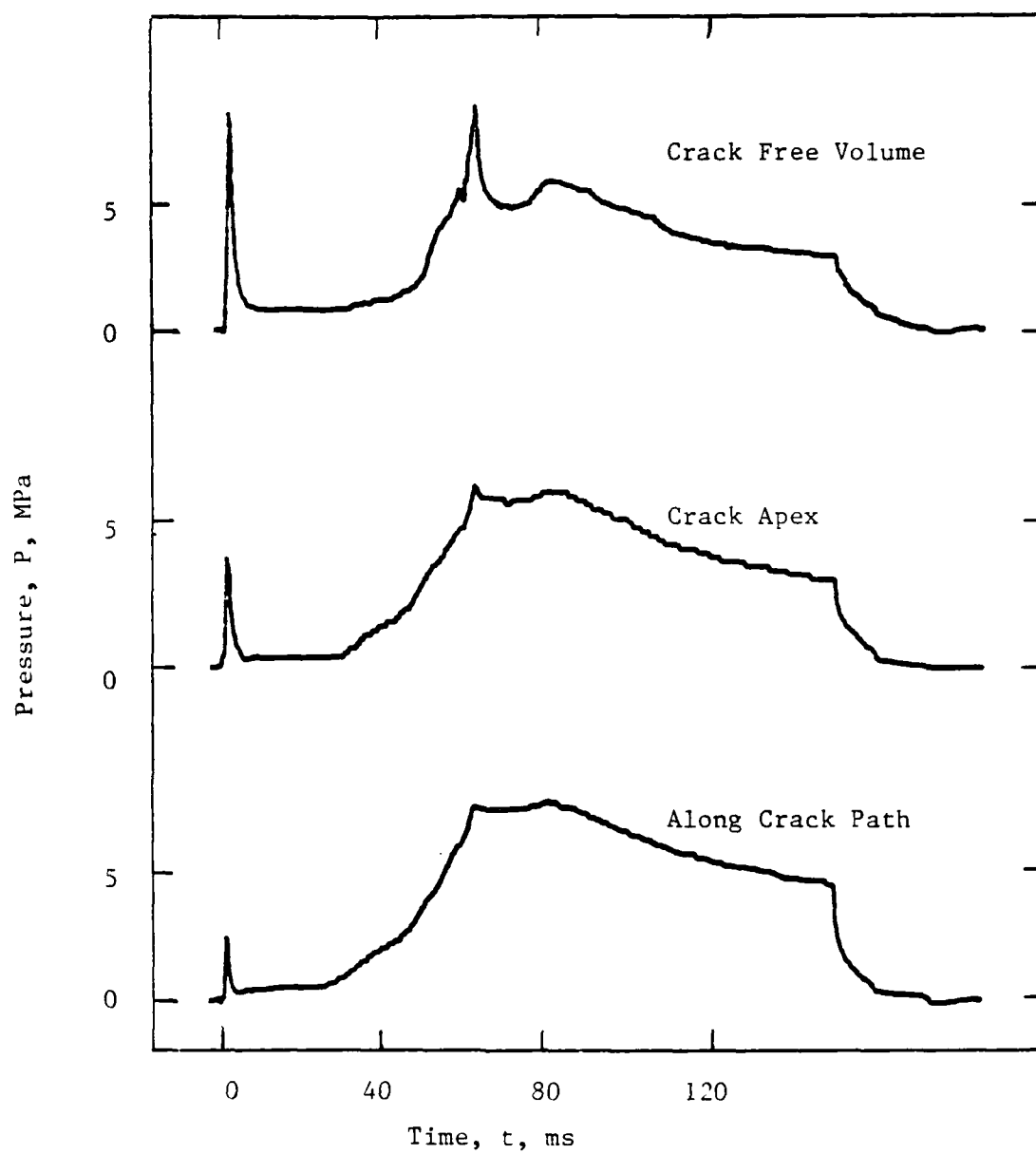
Fig. 14 Pressure-Time Trace for DNICP 40

rupture appeared to affect the peak pressure at the crack tip as it occurred during the depressurization of the free volume.

4.1.2 Interpretation of the Film Data

The degree of damage to the propellant sample was characterized by examining the film record of the event. A typical film record of a Mode B, single crack propagation is shown in Figure 15. Table I contains a frame-by-frame decription of the event. The instantaneous bright flame contours caused by burning in the crack are used to define the crack shape and length. From the contour (Figure 16), the crack tip location was measured as a function of time. Thus the crack velocity, extended length and number of macrocracks were deduced. In this test the initial crack length was longer than in previous tests. Figure 17 shows that the luminous flame front moved through the initially closed region and the crack propagation region at the same rate. The sharp reduction in propagation rate was caused by the depressurization of the chamber. A typical instantaneous bright flame contour for a branching experiment is shown in Figure 18.

4.1.3 Determining Other Key Parameters

In order to calculate each dimensionless parameter the values of r_b, K_{I_C} and E_{ref} must be determined. To represent the normal regression of the propellant surface in relation to the crack propagation, a steady state burning rate was calculated using Saint Robert's law[17]

$$r_b = aP^n \tag{34}$$

where P was the pressure at the time of crack initiation and a and n are burning rate constants given in Table II.[19]

0.2 ms   0.8 ms   1.4 ms

2.0 ms   2.6 ms   3.2 ms   3.8 ms
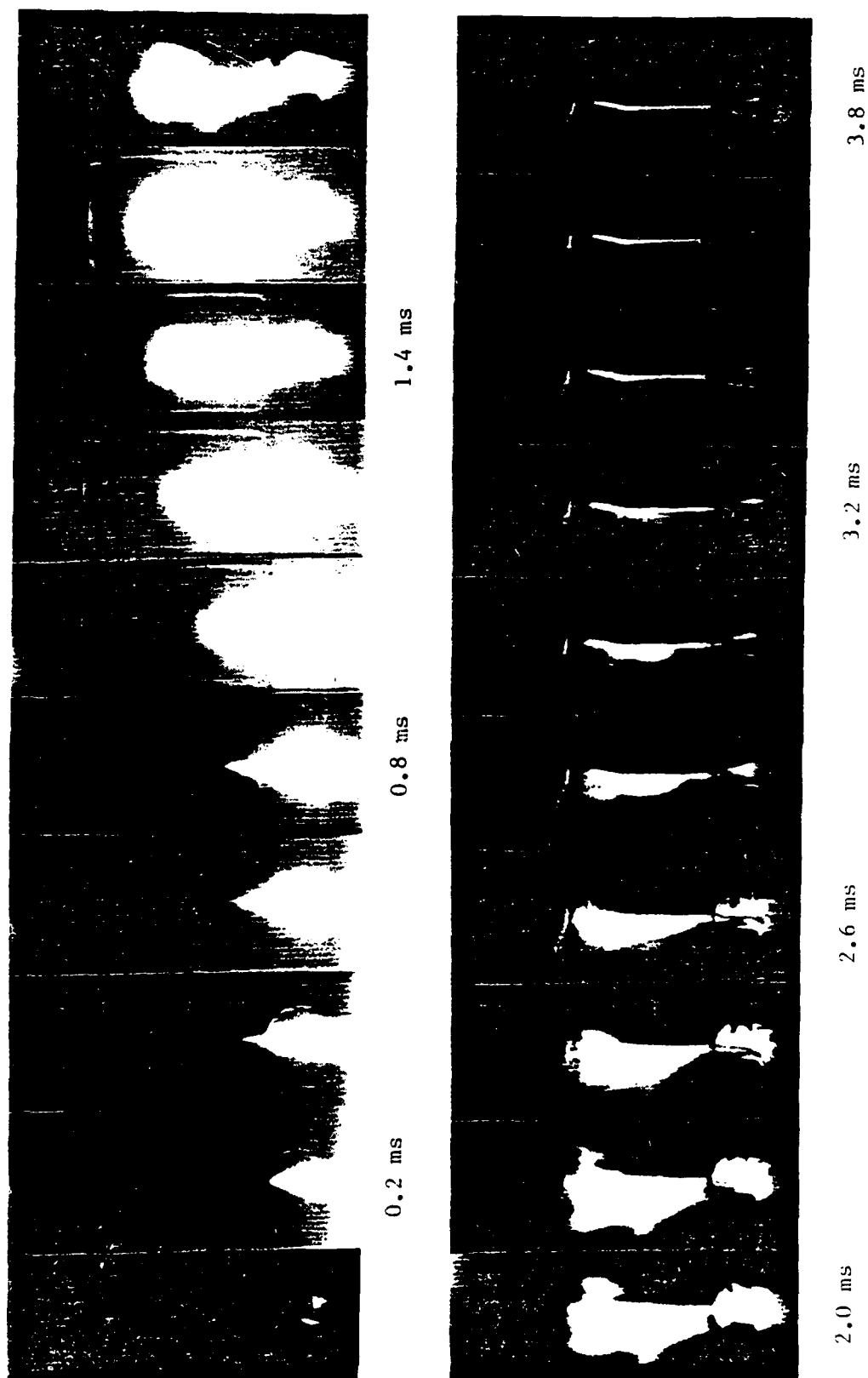
Fig. 15 Film Record from DNICP 40

Table I. Film Interpretation of Crack Propagation Process

Picture No.	Time (ms)	Event
1-6	0-0.6	Igniter gases fill crack cavity.
7-12	0.6-1.2	Flame penetrates precut crack.
13-16	1.2-1.6	A single crack propagates. High pressure gas continues to flow into crack region.
17-28	1.6-2.8	Crack cavity is clearly seen. Propagation has stopped.
29-34	2.8-3.4	Rupture disk bursts and flame intensity is reduced.
35-	3.4-	Propellant sample is not extinguished and burns completely.
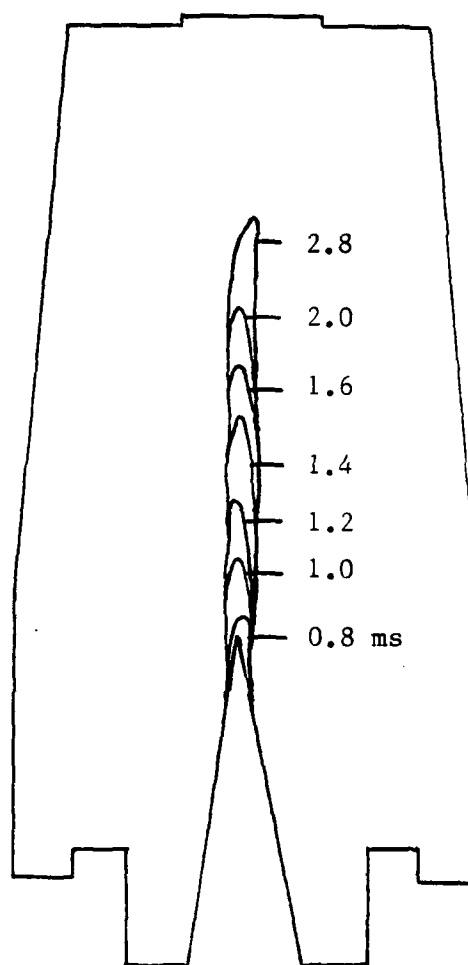
$$\partial P / \partial t = 12.0 \text{ GPa/s}$$
$$V_p = 35.4 \text{ m/s}$$
$$n = 1$$

Fig. 16   Instantaneous Bright Flame Front Contour
from DNICP 40
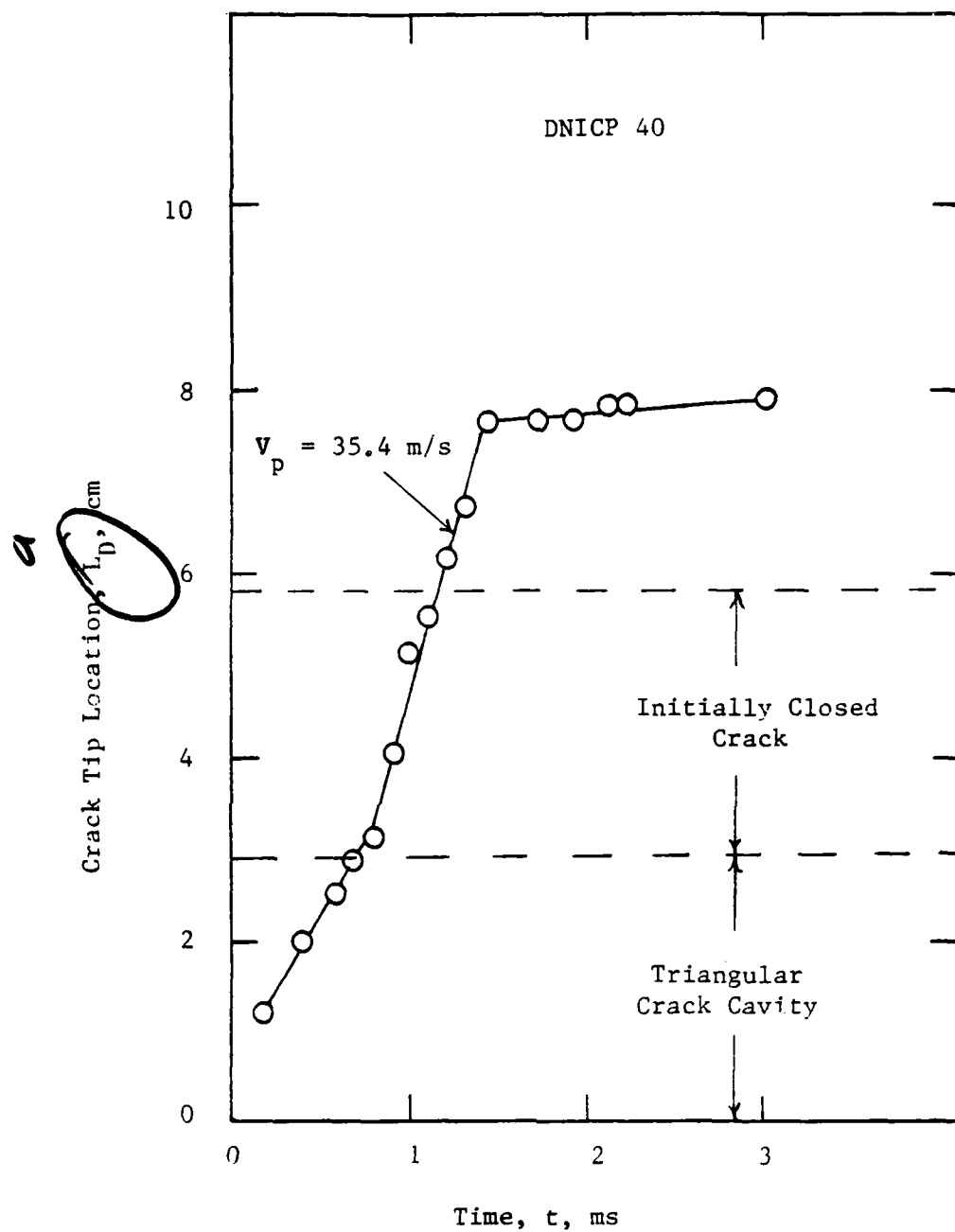
Fig. 17 Crack Tip Location versus Time
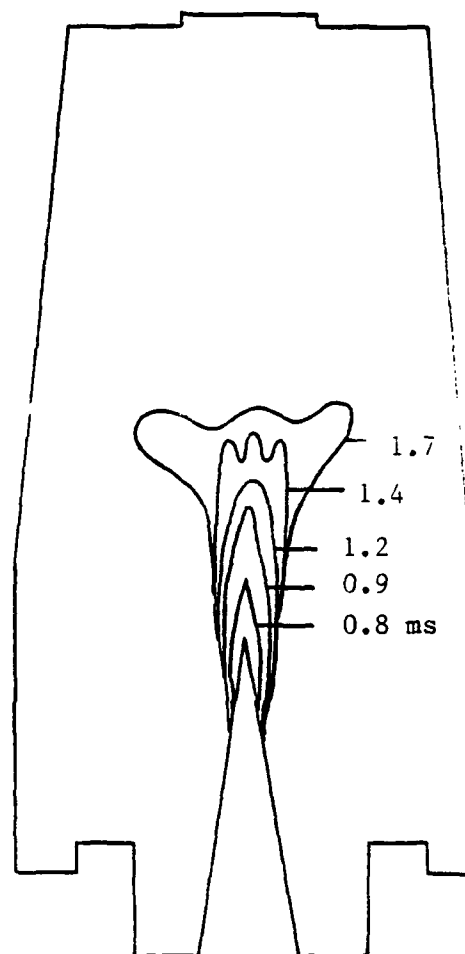
$$\partial P/\partial t = 49.0 \text{ GPa/s}$$
$$V_p = 29.0 \text{ m/s}$$
$$n = 3$$

Fig. 18 Instantaneous Bright Flame Front Contour
from DNICP 31

Table II. Steady State Burning Rate Constants

Type	a $(mm/s/(atm)^n$	exponent n
ARC 4525	0.5849	0.5427
ARC 5051	0.8441	0.5611

The critical stress intensity factor K_{I_c}, was calculated using
equations (9), (14) and the relationship

$$\sigma = P\cos\psi_i \tag{35}$$

The relaxation modulus E_{ref}, was taken from Figure 8 where t was the
time of crack initiation.

4.2 Relationships Between Dimensionless Parameters

Using the data obtained from numerous experiments, several sets of
values for the nine dimensionless parameters have been deduced (Table
III). With this data, the functional relationships of these parameters
were obtained statistically using a multiple regression analysis
program. The results can be expressed as

$$\pi_A = 20.697 \ \pi_E^{0.107}\pi_F^{0.181}a_T^{0.321}(\sin\psi_i)^{2.49}(\sin\psi_o)^{0.645} \tag{36}$$

$$\pi_B = 6.16\times10^{-7} \ \pi_E^{0.065}\pi_F^{0.254}a_T^{-0.78}(\sin\psi_i)^{-6.45}(\sin\psi_o)^{-0.985} \tag{37}$$

$$\pi_C = 7.389 \ \pi_E^{0.274}\pi_F^{0.042}a_T^{-0.021}(\sin\psi_i)^{1.14}(\sin\psi_o)^{-0.045} \tag{38}$$

$$\pi_D = 10.9\times10^{4} \ \pi_E^{0.217}\pi_F^{0.076}a_T^{0.478}(\sin\psi_i)^{2.05}(\sin\psi_o)^{-0.117} \tag{39}$$

It is important to note that although the exponents of π_E and π_F
are small compared to the other exponents, the values of these two
parameters are, in general, large compared to $\sin\psi_i$, $\sin\psi_o$ and a_T, and

Table III. Experimental Values of Dimensionless Parameters

Test No.	π_A	π_B	π_C	π_D	π_E	π_F	a_T	ψ_i	ψ_o
13	0.25	3.963	1	4420	0.309	2970	1.3	9.0	11.5
14	0.221	2.981	1	2420	0.115	1060	1.3	9.0	11.5
15	0.428	2.238	1	5960	1.077	6530	1.1	9.0	11.5
21	0.467	29.470	5	13490	18.930	186900	1.3	9.6	3.0
23	0.342	28.920	3	13400	8.160	110800	1.1	9.1	3.0
24	0.204	4.528	1	5940	0.439	3910	1.8	9.7	3.5
26	0.441	36.910	3	17000	18.300	132100	1.5	8.8	3.5
27	0.329	27.370	4	10250	13.120	41500	1.8	8.8	3.5
31	0.338	29.110	3	10900	15.310	79300	1.2	8.8	3.5
40	0.236	2.945	1	2720	0.473	3500	2.5	8.9	5.0

therefore have a dominant effect.

In order to check the reliability of these predictions, equations (36) through (39) are plotted with the values obtained from test data (Figures 19 through 22). These figures show that the predictions adequately characterize the experimental data. The multiple regression analysis calculated R^2 values greater than 89% for all correlations. R^2 is defined as the sample multiple coefficient of determination given by

$$R^2 = \frac{\Sigma(Y_i - \hat{Y}_i)^2}{\Sigma(Y_i - \bar{Y})^2} \tag{40}$$

where Y_i are the measured values, $\bar{Y}$ is the mean value of Y_i and $\hat{Y}_i$ is the predicted value of Y_i.

4.3 Discussion of Results

The expressions for π_A, π_B, π_C and π_D characterize the damage in the sample in terms of the extended macrocrack length, increase in burning surface area, number of macrocracks, and crack propagation velocity. From equations (36) through (39), the effects of the operating conditions characterized by π_E, π_F, ψ_o, ψ_i and a_T on the sample damage can be analyzed individually. The equations show that all damage parameters increase with π_E and π_F. The pressurization rate (π_F) is particularly dominant in extending the crack length and increasing the specific surface area. This agrees with previous studies[5-8] which showed an increase in damage for higher rates of thermal energy input and higher pressurization rates.

Changes in ψ_o change the confinement of the damaged zone allowing varying degrees of sample deformation. The equations predict that a
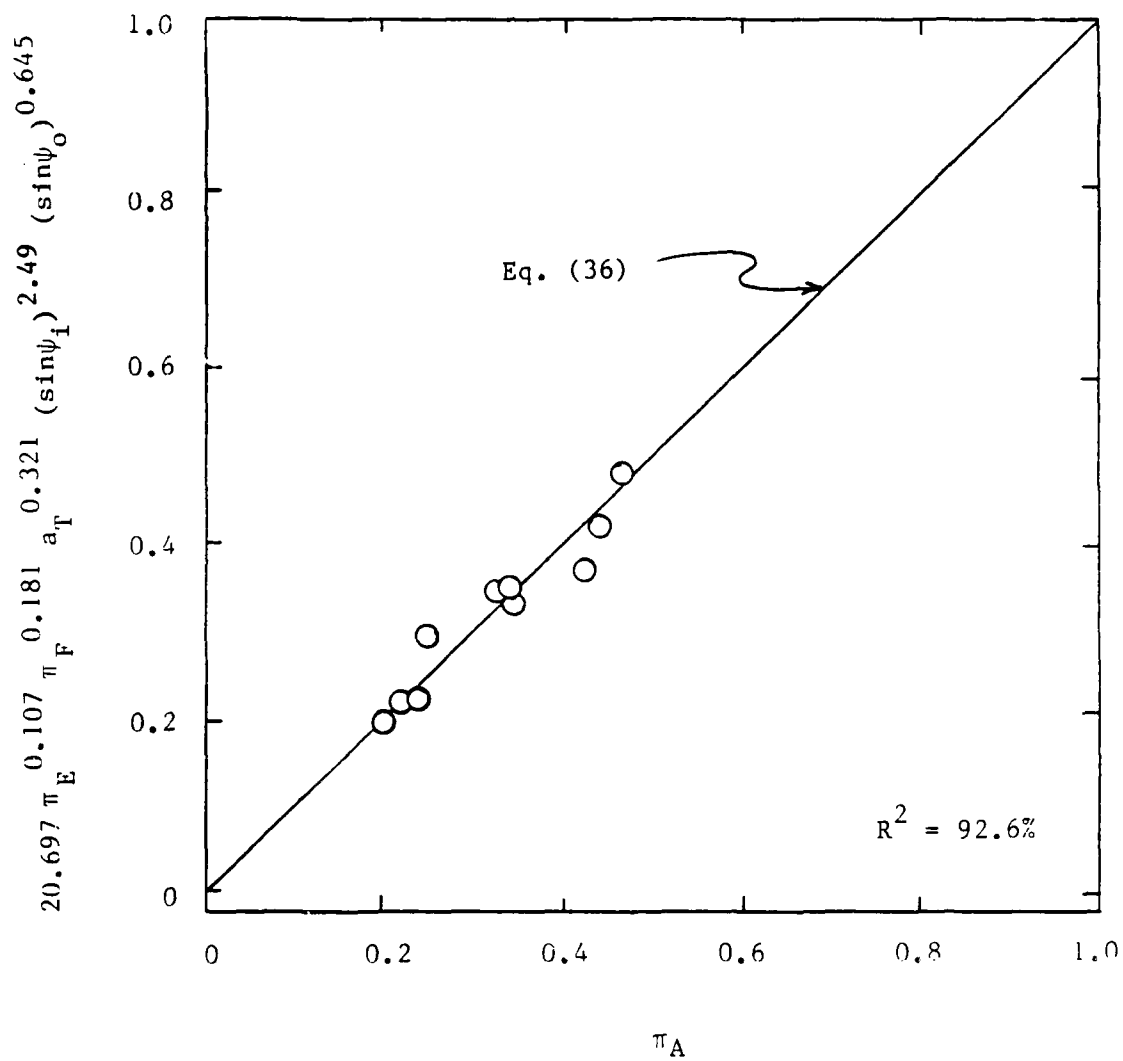
Fig. 19   Data Correlation for the Extended Crack Length π_A

The vertical axis is labeled $6.16 \times 10^{-7} \, \pi_E^{0.065} \, \pi_F^{0.254} \, a_T^{-0.78} (\sin\psi_i)^{-6.54} (\sin\psi_o)^{-0.985}$

Eq. (37)

$R^2 = 92.1\%$

π_B
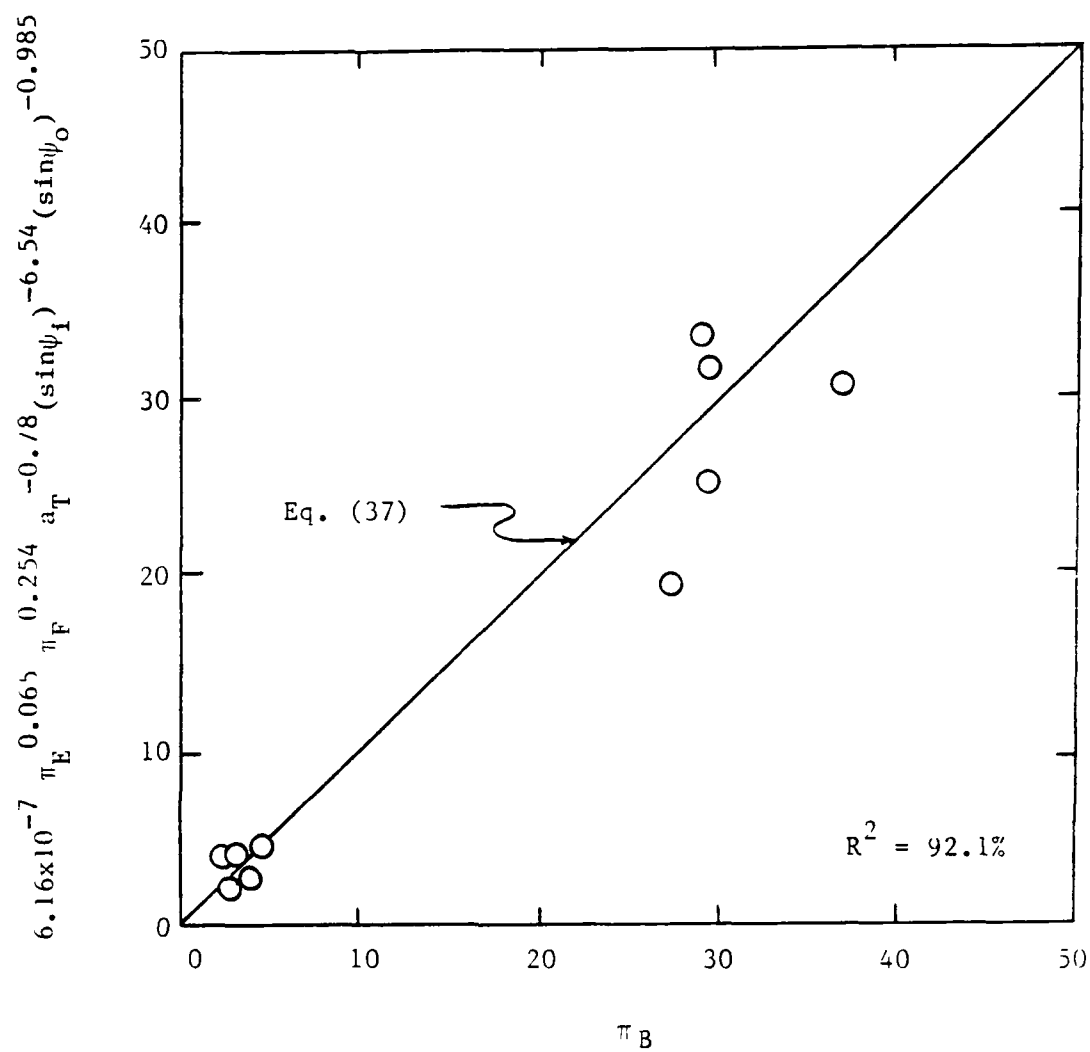
Fig. 20 Data Correlation for the Rate of Increases in Specific Surface Area π_B
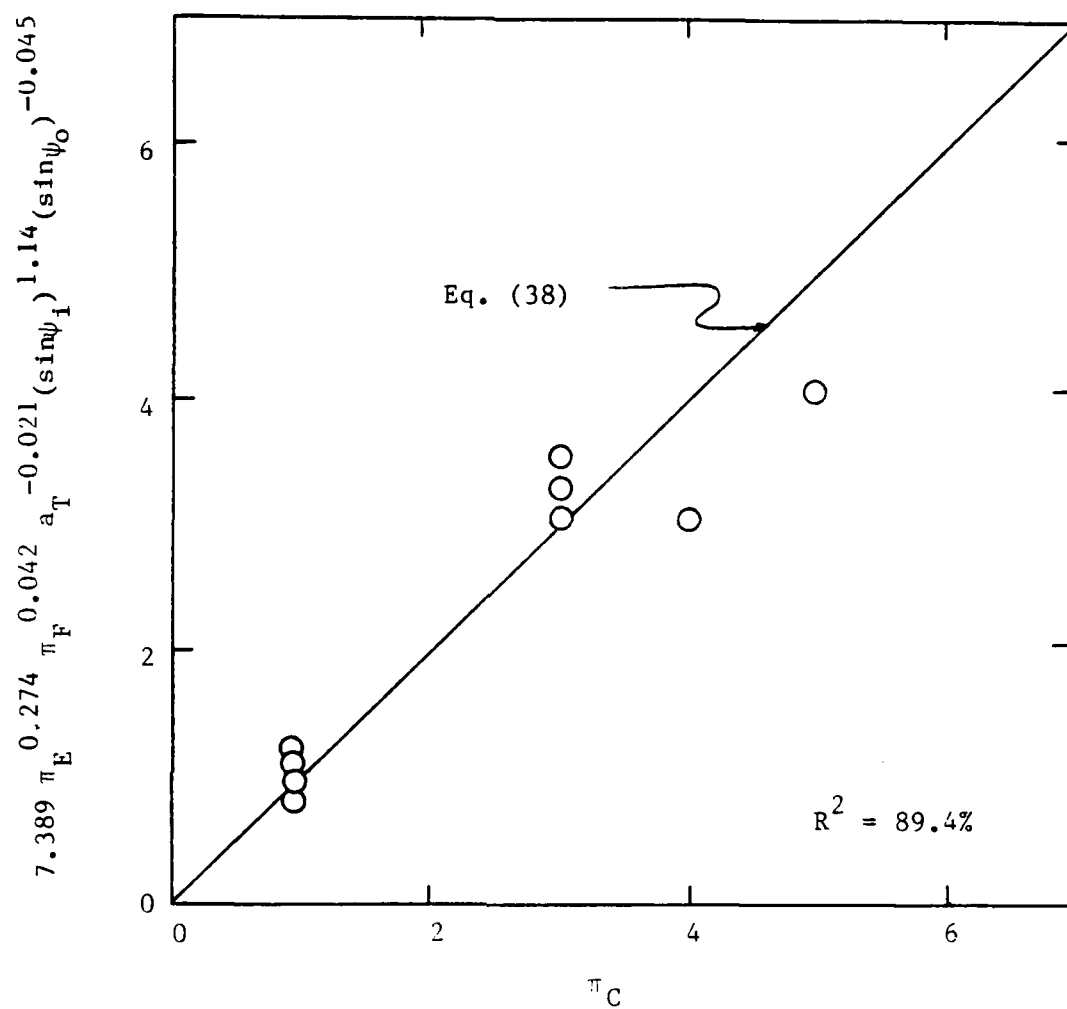
Fig. 21 Data Correlation for the Number of Macrocracks π_C

$10.9 \times 10^4 \ \pi_E^{0.217} \ \pi_F^{0.076} \ a_T^{0.478} (\sin\psi_I)^{2.05} (\sin\psi_o)^{-0.117}$

Eq. (39)

$R^2 = 92.7\%$

π_D
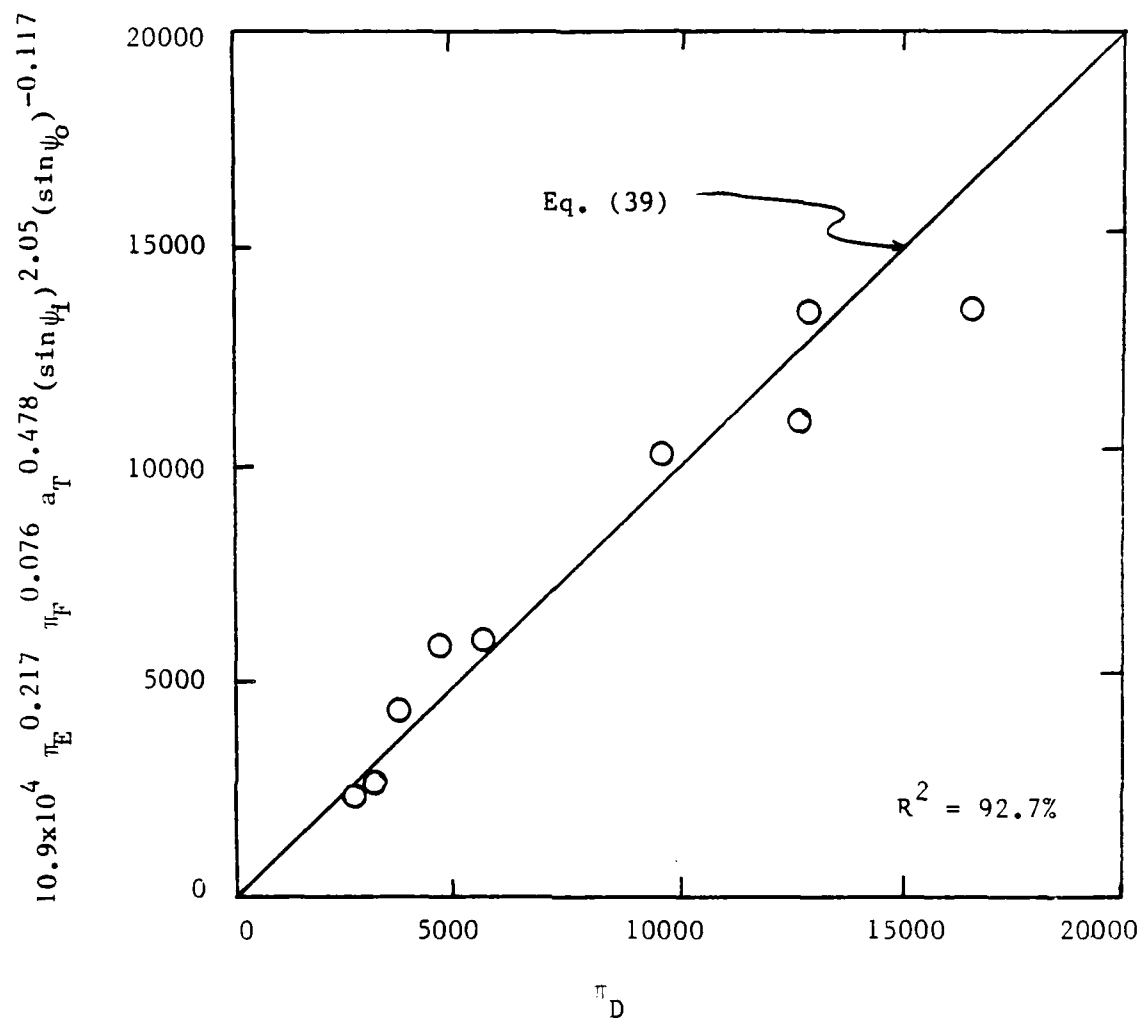
Fig. 22   Data Correlation for the Crack Propagation Velocity π_D

greater angle will increase crack growth while each of the other parameters will decrease. Under these conditions the angle at the crack tip is likely to be greater resulting in a higher local stress concentration. Thus, the single crack propagation mode is more probable. With a longer, single crack, equation (37) indicates that these two effects contribute to a decrease in π_B. Also, higher sample deformation work implies less energy is available to propagate the crack, reducing V_p.

The effects of initial propellant temperature on the crack propagation process can be very important. At lower temperatures (higher values of a_T) the propellant becomes more brittle, lowering its fracture energy. Higher crack velocities and longer cracks are expected. However, the range of initial temperatures in this study was limited by the test conditions. Broader ranges are needed to more accurately predict its effect. ψ_i was essentially unchanged in these tests but was included for the completeness of the correlations.

The agreement of these predictions with previous observations and basic principles in fracture mechanics indicates that the methodology for their development is valid. Similar correlations for different propellant types with different crack configurations could be developed using this method to determine guidelines for the safe operation of high performance rocket motors.

Chapter 5

SUMMARY AND CONCLUSIONS

Two types of composite propellants were selected for this study
(ARC 5051 and ARC 4525). They have similar composition but different
oxidizer particle sizes and mechanical properties. Several tests were
conducted under different loading conditions and sapmle geometries.
The damage to the sample was measured in terms of crack length, number
of cracks and crack propagation velocity. Using a dimensional analysis
of the key variables involved in the crack propagation phenomena, a set
of governing dimensionless parameters were established. These
parameters can provide some insight into the cause and effect
relationship between the momentum and energy input to a propellant
sample with existing flaws and the resultant damage.

Correlations of the dimensionless parameters were obtained by
performing a multiple regression analysis on the test data. The
driving parameters, π_E and π_F have positive relationships with the
damage parameters π_A, π_B, π_C and π_D. This indicates that higher
momentum and energy inputs to the crack cavity will cause a greater
degree of damage. The geometry and initial temperature of the
propellant sample have additional effects characterized by the
correlations. These correlations are only valid for the small ranges
of temperature and crack cavity angles studied; however, additional
tests could expand the applicability and validity of this method.
Enough data has been obtained to predict the strong dependence on the
rate of energy input and pressurization on crack propagation. The good
agreement with test data and reasonable physical interpretation

suggests that the methodology outlined in this study can provide a basis for future development of similar correlations defining safe operating conditions for solid propellant rockets.

Future research in this area should include:

a) development of correlations for high-energy propellants used in actual propulsion systems today, including high-elongation propellants;

b) extension of the present analysis to include propagation and flame spreading along a motor casing due to an initially debonded area, and;

c) integration of a crack/debond model into the Rocket Performance Prediction Code.

REFERENCES

1. Kumar, M. and Kuo, K. K., "Ignition of Solid Propellant Crack Tip Under Rapid Pressurization," AIAA Journal, Vol. 18, No. 7, July 1980, pp. 825-833.

2. Knauss, W. G., "On the Steady Propagation of a Crack in a Viscoelastic Sheet: Experiments and Analysis," Deformation and Fracture of High Polymers, edited by H. H. Kausch, J. A. Hassel and R. I. Jaffee, Plenum Press, 1974.

3. Schapery, R. A., "A Theory in Crack Initiation and Growth in Viscoelastic Media, I. Theoretical Development," Int. J. Fracture, Vol. 11, Feb. 1975, pp. 141-159.

4. Schapery, R. A., "A Theory in Crack Initiation and Growth in Viscoelastic Media, II. Approximate Methods of Analysis," Int. J. Fracture, Vol. 11, June 1975, pp. 369-388.

5. Schapery, R. A., "A Theory in Crack Initiation and Growth in Viscoelastic Media, III. Analysis of Continuous Growth," Int. J. Fracture, Vol. 11, Aug. 1975, pp. 549-562.

6. Siefert, J. G. and Kuo, K. K., "Crack Propagation in Burning Solid Propellants," Dynamics of Shock Waves, Explosions and Detonations, edited by J. R. Bowen, N. Manson, A. K. Oppenheim and R. I. Soloukhin, Vol. 94 of Progress in Astronautics and Aeronautics, 1985, pp. 575-595.

7. Kuo, K. K. and Moreci, J. A., "Crack Combustion and Branching in Burning Solid Propellants," 21st International Combustion Symposium, 1987.

8. Kuo, K. K., Moreci, J. A. and Mantzaras, J., "Different Modes of Crack Propagation in Burning Solid Propellants," J. Propulsion and Power, Vol. 3, No. 1, Jan.-Feb 1987, pp. 19-25.

9. Gent, A. N. and Marteny, P., "The Effect of Strain upon the Velocity of Sound and the Velocity of Free Retraction for Natural Rubber," ONR Technical Report No. 16, University of Akron, 1982.

10. De Luca, L., "Extinction Theories and Experiments," AIAA Progress Series, Vol. 90, edited by K. K. Kuo and M. Summerfield, 1984.

11. Kuo. K. K., Moreci, J. A., Kim, J. U., Torikai, T., Grubelich, M., Chang, L. K. and Beelitz, P., "Crack Propagation and Branching in Burning Solid Propellants and Ignition of Nitramine-Based Composite Propellants," Annual Report to Office of Naval Research Power Program, Jan. 1986, 114 pages.

12. Harbert, B. C. and Schapery, R. A.," Some Mechanical Properties of Two HTPB Composite Solid Propellants," Report No. MM 5222-86-20, Texas A&M University, 1986.

13. Mueller, H. K. and Knauss, W. G., "Crack Propagation in a Linearly Viscoelastic Strip," J. Applied Mechanics, June 1971, pp. 141-158.

14. Schapery, R. A., "Fracture Mechanics of Solid Propellants," Fracture Mechanics, edited by N. Perrone, H. Liebowitz, D. Mulville and W. Pilkey, U. Press of Va., 1978, pp. 387-398.

15. Langlois, G. and Gonard, R., "New Law for Crack Propagation in Solid Propellant Material," J. Spacecraft, Vol. 16, No. 6, Nov.-Dec. 1979, pp. 357-360.

16. Krier, H., "Solid Propellant Burning Rate During a Pressure Transient," Combustion Science and Technology, Vol. 5, 1972, pp. 69-73.

17. Cornelisse, J. W., Schoyer, H. F. R. and Walker, K. F., Rocket Propulsion and Spaceflight Dynamics, The Pitman Publishing Co., London, 1979, pp.174-179.

18. White, F. M., Fluid Mechanics, 2nd edition, McGraw-Hill Book Co., 1986, pp. 253-259.

19. Kumar, M., Kovacic, S. M. and Kuo, K. K., "Gas Penetration, Flame Propagation, and Combustion Processes in Solid Propellant Cracks," AIAA-80-1206, July 1980

20. Velikanov, M. A., Measurement Errors and Empirical Relations, Israel Program for Scientific Translations Ltd., 1965, pp. 172-177.

APPENDIX A

TEST PROCEDURES AND CHECKLIST FOR CRACK PROPAGATION TESTS

A. Igniter Assembly:

_____ 1. Cut igniter charge and record mass and propellant type.

_____ 2. Select a primer with a resistance 20 - 50 ohms and record.

_____ 3. Assemble primer, primer holder and lexane insulator.

_____ 4. Check primer resistance. If it has changed significantly, check leads and reassemble.

_____ 5. Place desired amount of propellant shavings in and around the primer.

_____ 6. Assemble remaining igniter pieces with the yellow marks aligned.

_____ 7. Check igniter circuit continuity.

_____ 8. Short igniter leads.

B. Sample preparation:

_____ 1. Measure and record the mass and dimensions of the sample.

_____ 2. Paint a dot on the front surface of the propellant for focusing purposes.

_____ 3. If Spin Physics camera will be used, mark the crack tip location with paint and measure distance between crack tip and focusing dot.

C. Chamber Assembly:

_____ 1. Install the desired N_2 inlet lines (except on igniter) and check for unobstructed flow.

_____ 2. Assure sacrificial and main windows properly fit into test chamber and clean window surfaces.

_____ 3. Spread flame retardant grease over all sample surfaces (except crack surface) and install in test chamber.

_____ 4. Insure propellant sample will not extend beyond sample holders when compressed.

_____ 5. Install main O-ring with joined ends at the rear of the chamber. Apply permatex to O-ring and groove .

_____ 6. Install sacrificial window against the propellant sample.

_____ 7. Install the main window into the chamber window cover.

_____ 8. Bolt the chamber window assembly to the main chamber, being careful to evenly compress the sample.

_____ 9. Measure and record top bursting diaphragm thickness and install diaphragm and hood assembly to top of chamber. Check for proper alignment of diaphragm holder to allow maximum flow area.

----- 10. Check side rupture disk and replace if necessary.

_____ 11. Install igniter assembly to bottom of chamber being sure to align the yellow marks. Check igniter resistance and short the igniter circuit.

_____ 12. Connect N_2 line to igniter. If not used, ensure that igniter ports are plugged.

D. Instrumentation:

_____ 1. Verify that all ignition circuits are in the off position.

_____ 2. Install pressure transducers and record their respective locations, sensitivities, and data lines.

_____ 3. Connect water lines and check for leaks. Turn off water supply.

_____ 4. Set up Hycam and install dummy film. Insure the film speed is reduced for ignition circuit test.

_____ 5. Connect volt-meter to ignition box and run ignition test.

_____ 6. Check focus of the Hycam.

_____ 7. Load new film, depress microswitch, and insure triggering arm operates properly as the camera door is secured. Reset PPS dial.

_____ 8. Check and record all camera settings.

_____ 9. Record test cell temperature.

_____ 10. Setup and focus Spin Physics camera (if used).

_____ 11. Remove lights used for focusing.

_____ 12. Install exaust fan and connect to Lights No. 1 receptacle.

_____ 13. Check data line connections to charge amplifiers.

_____ 14. Set input voltages and calibrate charge amplifiers.

_____ 15. Connect charge amplifier output to Physical Data recorder and record settings. Turn on Physical Data unit and hit reset button.

E. Test firing procedure:

    1. Perform final check of all connections.

_____ Hycam   _____ Spin Physics

_____ Transducers   _____ Water connections

_____ Exhaust fan   _____ N_2 lines

_____ Physical Data   _____ Charge Amps

_____ 2. Open outside door.

_____ 3. Secure safety key.

_____ 4. Connect igniter leads to igniter box.

_____ 5. Check igniter resistance.

_____ 6. Close and secure test cell door.

_____ 7. Turn on warning light and sound test alarm.

_____ 8. Verify charge amps are in CHARGE position.

_____ 9. Turn on igniter power and charge capacitor.

_____ 10. Turn on ignition panel switches 3 thru 6 and event switch.

_____ 11. Turn off safety switch.

_____ 12. Unground charge amplifiers, reset Physical Data recorder.

_____ 13. Turn on Spin Physics Camera and wait for ready light.

_____ 14. Turn on ignition switch.

_____ 15. After rupture disk bursts, inject N_2.

_____ 16. When propellant has stopped burning, stop Spin Physics camera.

F. Post Firing Procedures:

_____ 2. Ground charge amplifiers.

_____ 3. Turn off all ignition switches and turn on exhaust fan switch.

_____ 4. Make a hard copy of pressure traces on X-Y plotter.

_____ 5. Transfer pressure data to Nicolet and store on floppy disk.

_____ 6. Generate calibration signals for transducers and record on X-Y plotter.

DATA SHEET FOR CRACK PROPAGATION EXPERIMENTS

CRACK PROPAGATION TEST NO. _____

DATE _____

Participants:_____,_____,_____,_____,_____

TEMPERATURE: T(room) _____C   T(cell) _____C

CRACK GEOMETRY AND SAMPLE SPEC.:   IGNITER:

    Propellant type_____   Primer _____

    Configuration _____   Propellant type_____

    Length _____   Dimensions _____

    Max gap width _____   Mass _____

    Inner taper angle _____   Resistance _____

    Taper heigth _____

    Thickness _____   FLYING PIN IGNITER:

    Weight _____   Primer resistance_____

    Fuse Wire Location _____   Propellant weight_____

                                        Propellant type_____

CAMERA: Diaphragm thickness_____

    Type of Lens _____   Diaphragm diameter_____

    Framing Rate_____Frames/s   Diaphragm material_____

    Optical Head: 1/4 , 1/2 , frame

    PPS Dial _____   RUPTURE DISK ACTUATOR:

    Multiplier _____   Primer resistance_____

    Time Marker _____Pulses/s   Propellant weight_____

    Remote firing at_____ft   Propellant type _____

    Distance of focus_____ft

    Brake Dial_____   FILM:

    Servo_____   ASA No. _____

    H/L speed reducer_____   Length _____

    F. Stop:_____   Color _____, B & W _____

APPENDIX B

ERROR ANALYSIS

In the multiple regression of the data in Table II, the
exponential relationships assumed for the dimensionless parameters
[equations (36) through (39)] were rearranged into a linear
relationship based on the natural logarithm of each value. Using the
basic properties of logrithmic representations, the uncertainty in each
dimensionless quantity can be expressed as

$$\ln(x_i) = \ln(x) + e(x)/x \qquad (41)$$

where x_i is the actual value, x is the measured value and e(x) is the
error interval associated with that measurement.[20] The method of least
square analysis used on the measured data will give more accurate
results when

$$\ln(x) \gg e(x)/x \qquad (42)$$

An expression for the relative error in each dimensionless parameter is

$$r_x = e(x)/(x\ln(x)) \qquad (43)$$

Table IV contains estimations of the various errors involved in
measuring each of the variables in the experimental setup. Equation
(43) can then be evaluated for each of the dimensionless parameters.
This equation indicates that for values of x which approach unity, the
relative error could be significant. Since the error of π_c (n) is
assumed to be zero, its correlation is not affected. However, a_T does
have a finite error associated with it. For the worst case of

a_T = 1.1, r_x = 0.095 or 9.5% relative error. This could be improved by referencing a_T to a temperature outside the normal operating range.

Using equation (43) and the values listed in Table 4, the relative error was calculated for each dimensionless parameter based on its average value.

$$\pi_A = L_D/a_o \qquad (27)$$

Assume $e(L_D) \ll e(L_D)$ therefore $e(\pi_A)/\pi_A = e(L_D)/L_D$. Based on the average value, π_A = 0.326, r_{π_A} = 9.9%.

Using this method, the following values of r_x are obtained:

r_{π_A} = 9.9%

r_{π_B} = 3.9%

r_{π_C} = 0.0%

r_{π_D} = 0.3%

r_{π_E} = 1.7%

r_{π_F} = 3.4%

$r_{\sin\psi_i}$ = 5.9%

$r_{\cos\psi_o}$ = 8.2%

r_{a_T} = 2.1%

Table IV. Estimation of Measurement Errors

Physical Variable	Source and Type of Error	Error Interval (+/-)
ψ_i ψ_o	Random error in the measurement and calculation of the inner taper angle.	0.2°
	The systematic error of symmetry	0.5°
a_T	Random error in the measurement of the room temperature	0.5 K
	Systematic error in the difference between room temp. and initial propellant temp.	3.0 K
	Random and systematic error in converting temperature to a_T (note: in the temperature range of interest da_T/dT is near zero)	0.01
	Accuracy of the a_T data (note: a_T is defined near operating temperatures)	NA
n	Since n is a discrete quantity, it is assumed to have no random error	0.0
a_o	Random error of the measuring instrument	0.25 mm
L_D	Random error in determining the bright flame front tip location	2.0 mm
	Systematic error of correlation between the flame front and actual tip location (note: assumed to be small)	unknown
V_p	Random error of measuring the change of flame front location with respect to time (due to the averaging effect)	0.0
P	Systematic error of the installation, wear, calibration and recording of pressure data	5%
$\partial p/\partial t$	Since dp/dt is calculated using a very large dp and t is very accurate the error should not be greater than in P	5%